

Nonlocal *in-medium* effective interaction for nucleon scattering off isospin-asymmetric targets

J. I. Fuentealba-Bustamante

*Department of Physics-FCFM, University of Chile,
Av. Blanco Encalada 2008, RM 8370449 Santiago, Chile and
Department of Physics and Astronomy, Ohio University, Athens, Ohio 45701, USA*

H. F. Arellano

*Department of Physics-FCFM, University of Chile,
Av. Blanco Encalada 2008, RM 8370449 Santiago, Chile
(Dated: August 4, 2025)*

We have investigated the role of isospin asymmetry of the NN effective interaction in the context of NA elastic scattering. To this purpose we represent the *in-medium* g matrix as an admixture of isospin-symmetric nuclear matter and pure neutron matter solutions of Brueckner-Hartree-Fock equations for infinite nuclear matter, denoted as $g[\rho, \beta]$. We use the Argonne v_{18} bare potential to represent the NN interaction in free space, due to its ability to describe the NN scattering amplitudes up to 350 MeV. The density-dependent isospin-asymmetric g matrices are then used to calculate optical model potentials for elastic nucleon scattering off closed-shell nuclei. For this aim, we make use of the Arellano-Bauge δg -folding approach suited for an explicit treatment of nonlocal density matrices. This approach allows to account for the local isospin-asymmetry and density dependence of the *in-medium* NN interaction. The resulting optical potentials are nonlocal since the entire nonlocal structure of the g matrix is retained. We observe that including the isospin asymmetry in the g matrix allows for a reasonable description of differential cross-sections at nucleon beam energies between 40 and 200 MeV. In the case of proton scattering at energies below ~ 65 MeV, at momentum transfers q below $\sim 1 \text{ fm}^{-1}$, the inclusion of neutronic-matter g matrices yields better agreement with the data as compared to the case when symmetric nuclear matter g matrices are used. These results provide evidence that the isospin-asymmetry in the NN effective interaction yield non-negligible effects in nucleon scattering off isospin-asymmetric targets at beam energies below 65 MeV.

I. INTRODUCTION

Current efforts in nuclear research are being directed toward the study of nuclear systems with significant isospin asymmetry, resulting in renewed interest in the study of nuclei at the limits of stability. Along this line, radioactive ion beam accelerators play a central role in delivering high-intensity beams of rare isotopes to collide against selected targets. Facilities such as FRIB at MSU in the USA, GSI in Germany, EURISOL in Europe, ISOLDE at CERN, SPIRAL2 at GANIL in France, RIBF at RIKEN in Japan, and ISOL@MYRRHA in Belgium[1–6], constitute examples of these developments. In the case of an exotic beam colliding with a hydrogen target, the process becomes equivalent to nucleon-nucleus (NA) scattering. Indeed, inverse kinematics enables the reduction of a, e.g., 65A-MeV ion scattering off a hydrogen target to a 65-MeV proton scattering off the nucleus of the ion. In this context, optical model potentials for NA scattering constitutes a valuable tool for extracting information from scattering experiments involving rare isotope beams.

Considering that rare isotopes are exotic, featuring significant isospin-asymmetry, the detailed treatment of this effect must be guided by theory. Along this line, microscopic optical potentials are still a primary tool to explore untested domains, avoiding phenomenological extrapolations. In this vein, significant developments have taken place such as *ab-initio* calculations of optical potentials for low energy neutron scattering [7–9] and *ab-initio* folding potentials based on the Watson expansion [10, 11]. See Refs. [12, 13] for up-to-date reviews on the subject. In this work we focus explicitly on accounting for the isospin asymmetry of the nuclear medium in the representation of the *in-medium* nucleon-nucleon (NN) effective interaction.

The work we present here is an extension of the parameter-free optical model introduced by Arellano and Bauge in 2007 [14, 15], where the optical potential keeps track of a site-dependent effective interaction. In the model, Brueckner-Hartree-Fock (BHF) g -matrices have been used to represent the *in-medium* NN interaction, although limited to the use of isospin-symmetric nuclear matter.

In the calculation of the optical potential for nucleon scattering from a given nucleus, the isospin asymmetry gets manifested by two elements. One of them comes from the one-body density matrix for the target protons and neutrons, whereas the other stems from the local isospin asymmetry at the site where the NN interaction takes place. Current microscopic schemes for calculating microscopic optical potentials, make use of isospin-symmetric g matrices, thus

neglecting the asymmetry of the medium. We aim to go beyond this approach by accounting explicitly for the isospin asymmetry in the NN interaction. By incorporating explicitly g matrix solutions for pure neutron (proton) matter, the g matrix becomes a functional of the isoscalar density ρ and isospin asymmetry β , to be expressed as $g[\rho, \beta]$.

Investigations on the density and asymmetry dependence of g matrices within BHF approximation have been reported in Refs. [16–18]. For this work, we refer to the article by Bombaci and Lombardo, where they report BHF calculations of considering various asymmetries $\beta = (N - Z)/A$. The interesting finding they report is that the depth of the single-particle (s.p.) potentials for protons and neutrons vary nearly linearly as functions of β , with $0 \leq \beta \leq 1$. Since the s.p. self-consistent potentials correspond to the on-shell mass operator, which in turn scales with the g matrix, we can then assume that the g matrix varies –to lowest order– linearly as a function of β . We apply this linear behavior in the construction of the g matrix, and interpolate the solutions for symmetric nuclear matter ($\beta = 0$) and pure neutron matter ($\beta = 1$) linearly. This construction enables us to assess the role of the isospin asymmetry in the microscopic calculation of optical potentials for isospin-asymmetric targets such as ^{48}Ca , ^{90}Zr and ^{208}Pb . We will consider proton and neutron probes at energies up to 200 MeV. The bare interaction to be used is Argonne v_{18} (AV18) [19].

This article is organized as follows. In Section 2, we present the theoretical framework, where we review general aspects of the δg folding. We also introduce a model incorporating the isospin asymmetry in the NN effective interaction. In Section 3, we present the main considerations for the implementation of the δg folding. We also briefly outline the *in-medium* g matrix in BHF. In Section 4 we present results for proton and neutron elastic scattering from the isospin-asymmetric targets ^{208}Pb and ^{48}Ca . Section 5 summarizes the work and draws its main conclusions.

II. FRAMEWORK

The optical potential for NA scattering can be formulated in multiple ways. Most of them can be reduced to the expectation value of a generalized two-body effective interaction with the nucleus in its ground state [20–24]. With this observation, the optical potential in momentum space for the scattering of a nucleon of energy E from a nucleus can be expressed as

$$U(\mathbf{k}', \mathbf{k}; E) = \int d\mathbf{p}' d\mathbf{p} \langle \mathbf{k}' \mathbf{p}' | \hat{T}(E) | \mathbf{k} \mathbf{p} \rangle_{\mathcal{A}} \hat{\rho}(\mathbf{p}', \mathbf{p}), \quad (1)$$

where the subscript \mathcal{A} denotes antisymmetrization and $\hat{\rho}(\mathbf{p}', \mathbf{p})$ is the nonlocal one-body density matrix of the target. In this way, the information about the multi-nuclear nature of the system is contained in the \hat{T} matrix. In the above, \mathbf{k} and \mathbf{p} represent the momenta of the projectile and struck nucleon before the interaction, respectively. Analogously, \mathbf{k}' and \mathbf{p}' refer to the post-interaction momenta.

In quite general terms, it is shown in Ref. [14] that any two-body operator \hat{T} can be expressed in the following functional form

$$\langle \mathbf{k}' \mathbf{p}' | \hat{T} | \mathbf{k} \mathbf{p} \rangle = \int \frac{dz}{(2\pi)^3} e^{iz \cdot (\mathbf{Q} - \mathbf{q})} g_z(\mathbf{K} + \mathbf{P}; \mathbf{b}', \mathbf{b}), \quad (2)$$

where g_z is a reduced matrix which depends on the z coordinate. The above result comes after transforming $\langle \mathbf{k}' \mathbf{p}' | \hat{T} | \mathbf{k} \mathbf{p} \rangle$ to coordinate space, obtaining $\langle \mathbf{r}' \mathbf{s}' | \hat{T} | \mathbf{r} \mathbf{s} \rangle$, and then transforming it back to the momentum representation. In the process, \mathbf{z} is identified as the average coordinate of both prior and post coordinates, namely

$$\mathbf{z} = \frac{1}{4}(\mathbf{r} + \mathbf{s} + \mathbf{r}' + \mathbf{s}'). \quad (3)$$

Additionally,

$$\mathbf{b}' = \frac{1}{2}(\mathbf{k}' - \mathbf{p}'), \quad \mathbf{b} = \frac{1}{2}(\mathbf{k} - \mathbf{p}), \quad (4)$$

represent the pre- and post-collision relative momenta. Furthermore,

$$\mathbf{K} = \frac{1}{2}(\mathbf{k} + \mathbf{k}'), \quad \mathbf{q} = \mathbf{k} - \mathbf{k}', \quad (5)$$

represent the projectile average momentum and the momentum transfer. Likewise,

$$\mathbf{P} = \frac{1}{2}(\mathbf{p} + \mathbf{p}'), \quad \mathbf{Q} = \mathbf{p}' - \mathbf{p}, \quad (6)$$

account for the struck-nucleon average momentum and the recoil momentum.

Guided by folding models using density-dependent NN effective interactions [25–27], the authors in Ref. [28] assume g_z as the fully off shell *in-medium* g matrix for infinite nuclear matter. The density at which the g matrix is evaluated correspond to that at the coordinate z , namely $\rho(z)$. After replacing Eq. (2) for \hat{T} in Eq. (1) for U , we obtain

$$U(\mathbf{k}', \mathbf{k}; E) = \frac{1}{(2\pi)^3} \int d\mathbf{Q} d\mathbf{P} dz e^{iz \cdot (\mathbf{Q} - \mathbf{q})} \times g_z(\mathbf{K} + \mathbf{P}; \mathbf{b}', \mathbf{b}) \hat{\rho}(\mathbf{Q}; \mathbf{P}) \quad (7)$$

As observed, the optical potential involves multidimensional integrals, namely three-dimensional integrals over \mathbf{z} , \mathbf{Q} and \mathbf{P} . In Ref. [29], it was shown that a reasonable approximation to the above expression for U is setting $\mathbf{Q} = \mathbf{q}$ in the g matrix, so that the relative momenta become

$$\mathbf{b}' = \frac{1}{2}(\mathbf{K} - \mathbf{P} - \mathbf{q}); \quad \mathbf{b} = \frac{1}{2}(\mathbf{K} - \mathbf{P} + \mathbf{q}). \quad (8)$$

Additionally, the authors of Ref. [14] demonstrate that the optical potential can be expressed as the sum of two terms in the form

$$U(\mathbf{k}', \mathbf{k}; E) = U_0(\mathbf{k}', \mathbf{k}; E) + U_1(\mathbf{k}', \mathbf{k}; E), \quad (9)$$

where

$$U_0(\mathbf{k}', \mathbf{k}; E) = \int d\mathbf{P} \langle \mathbf{b}' | t | \mathbf{b} \rangle_{\mathcal{A}} \hat{\rho}(\mathbf{q}; \mathbf{P}); \quad (10a)$$

$$U_1(\mathbf{k}', \mathbf{k}; E) = \frac{-1}{6\pi^2} \int_0^\infty z^3 dz \int d\mathbf{P} \int d\mathbf{Q} \times \left[\frac{3 j_1(|\mathbf{Q} - \mathbf{q}|z)}{|\mathbf{Q} - \mathbf{q}|z} \right] \langle \mathbf{b}' | \frac{\partial g_z}{\partial z} | \mathbf{b} \rangle_{\mathcal{A}} \hat{\rho}(\mathbf{Q}; \mathbf{P}). \quad (10b)$$

Here, j_1 denotes the spherical Bessel function of first order. In calculations reported here, both t and g_z are evaluated at an average value of the pair momentum $\mathbf{K} + \mathbf{P}$. Note that the intrinsic medium effects get manifested as the gradient of g_z at the (mean) average coordinate z . This feature of the model motivates to refer to it as δg folding.

Note that if the reduced interaction g_z is translationally invariant, as is the case for the free t matrix, then $\partial g_z / \partial z = 0$, so that U_1 vanishes. The resulting potential reduces to U_0 , corresponding to the medium-free full folding potentials reported in Refs. [30–34].

An interesting property which emerges from the above expression for U is that if the density matrix is expressed in the Slater approximation (See appendix A), then U gets reduced to [14]

$$U_{\text{ABL}}(\mathbf{k}', \mathbf{k}; E) = 4\pi \int_0^\infty z^2 dz j_0(qz) \rho(z) \langle g_z^{(0)}(\mathbf{k}', \mathbf{k}) \rangle. \quad (11)$$

In this expression $\langle g_z(\mathbf{k}', \mathbf{k}) \rangle$ represents the Fermi-motion integral

$$\langle g_z(\mathbf{k}', \mathbf{k}) \rangle = \int d\mathbf{P} n_z(P) g_z(\mathbf{K} + \mathbf{P}; \mathbf{b}', \mathbf{b}). \quad (12)$$

Here, $n_z(P)$ is given by Eq. (A10), setting bounds for the off-shell sampling of the interaction g_z at density $\rho(z)$. From now on, we shall refer to this expression for the optical potential as ABL folding, in reference to its authors [28]. This expression has become useful for us to check the subroutines coded in this work. The g matrix is evaluated at a starting energy $\omega = E + \bar{e}$, with E being the kinetic energy in the NA center of mass (c.m.), and \bar{e} an average nuclear-matter s.p. energy at the local density $\rho(z)$.

To incorporate the isospin asymmetry in the g matrix, we proceed as follows. Let $\rho_p(z)$ and $\rho_n(z)$ be the point proton and neutron densities, respectively. Then, we define the isoscalar density as

$$\rho(z) = \rho_p + \rho_n. \quad (13)$$

Additionally, to characterize the isospin asymmetry at each radial site z in the nucleus we define the local isospin

asymmetry $\beta(z)$ as

$$\beta(z) = \frac{\rho_n - \rho_p}{\rho_n + \rho_p}. \quad (14)$$

Considering the density-dependent g matrix a functional of the isoscalar density ρ and isospin asymmetry β , then $g = g[\rho, \beta]$. As justified in Sec. I, the dependence of the g matrix on the asymmetry is assumed to be linear. Thus, if $g^{(0)}[\rho]$ denotes the g matrix in symmetric nuclear matter (SNM), and $g^{(1)}[\rho]$ denotes the one for pure neutron matter (PNM), then functional dependence of g on ρ and β gets expressed as

$$g[\rho, \beta] = g^{(0)}[\rho] (1 - \beta) + g^{(1)}[\rho] \beta. \quad (15)$$

Note that if the medium is nearly isospin symmetric, as in ^{40}Ca , $\beta \approx 0$, so that $g[\rho, \beta] \approx g^{(0)}[\rho]$. In the other extreme, such as in neutron stars, then $\beta \approx 1$, so that $g[\rho, \beta] \approx g^{(1)}[\rho]$.

To calculate U_1 from Eq. (10b) we need to evaluate the gradient term $\partial g / \partial z$ at each coordinate z . Consistent with Eq. (15) we get

$$\frac{\partial g}{\partial z} = \left[\frac{\partial g^{(0)}}{\partial z} (1 - \beta) - g^{(0)} \frac{\partial \beta}{\partial z} \right] + \left[\frac{\partial g^{(1)}}{\partial z} \beta + g^{(1)} \frac{\partial \beta}{\partial z} \right], \quad (16)$$

where

$$\frac{\partial g^{(0)}}{\partial z} = \frac{\partial g^{(0)}[\rho]}{\partial \rho} \frac{\partial \rho(z)}{\partial z}, \quad (17a)$$

$$\frac{\partial g^{(1)}}{\partial z} = \frac{\partial g^{(1)}[\rho]}{\partial \rho} \frac{\partial \rho(z)}{\partial z}. \quad (17b)$$

To illustrate the behavior of the isospin-asymmetry $\beta(z)$ for nuclei of interest, in Fig. 1 we show the isoscalar density ρ (a), the isospin-asymmetry β (b) and its dimensionless gradient $z(\partial\beta/\partial z)$ as functions of the radial coordinate z . Solid, short-dashed, and long-dashed curves correspond to ^{208}Pb , ^{90}Zr and ^{48}Ca , respectively. The vertical lines in panel (a) denote the root-mean-squared (rms) radius for each nucleus.

We observe that the isoscalar point densities $\rho(z)$ displayed in panel (a) are nearly constant up to about their respective rms radius. Beyond that point the density decreases rapidly as the radial coordinate increases. It is also interesting to note that both β and $z(\partial\beta/\partial z)$ for ^{90}Zr are rather small compared to the other two nuclei. This feature points to that the role of $g^{(1)}[\rho]$ in the optical potential for ^{90}Zr as target would be marginal, as inferred from Eq. (16) for U_1 .

III. IMPLEMENTATION

A. Target ground state

For the actual calculation of the optical potential, we need to describe the target in its ground state. For this purpose, we use shell-model single-particle (s.p.) wavefunctions based on a computational code furnished by J. Negele [35]. These correspond to self-consistent Hartree-Fock calculations in the local density approximation.

In Fig. 2 we show the s.p. wavefunctions $R_{nlj}(z)$ as functions of the radial coordinate z for ^{48}Ca . Here n denotes the principal quantum number, l the orbital angular momentum and j the total angular momentum. This is a spherical nucleus composed of twenty protons and twenty-eight neutrons. As a result, there are six and seven shells, respectively. Black, red, blue, and green curves denote s , p , d and f waves. Note that only the s shell has two bound states, with the second one featuring a node around 2.5 fm (black dashed curves). The root-mean-squared radii for proton and neutron densities are 3.46 and 3.65 fm, respectively.

In terms of the s.p. wavefunctions of the nucleus, the point density is given by

$$\rho(z) = \sum_{nlj} (2j+1) |R_{nlj}(z)|^2, \quad (18)$$

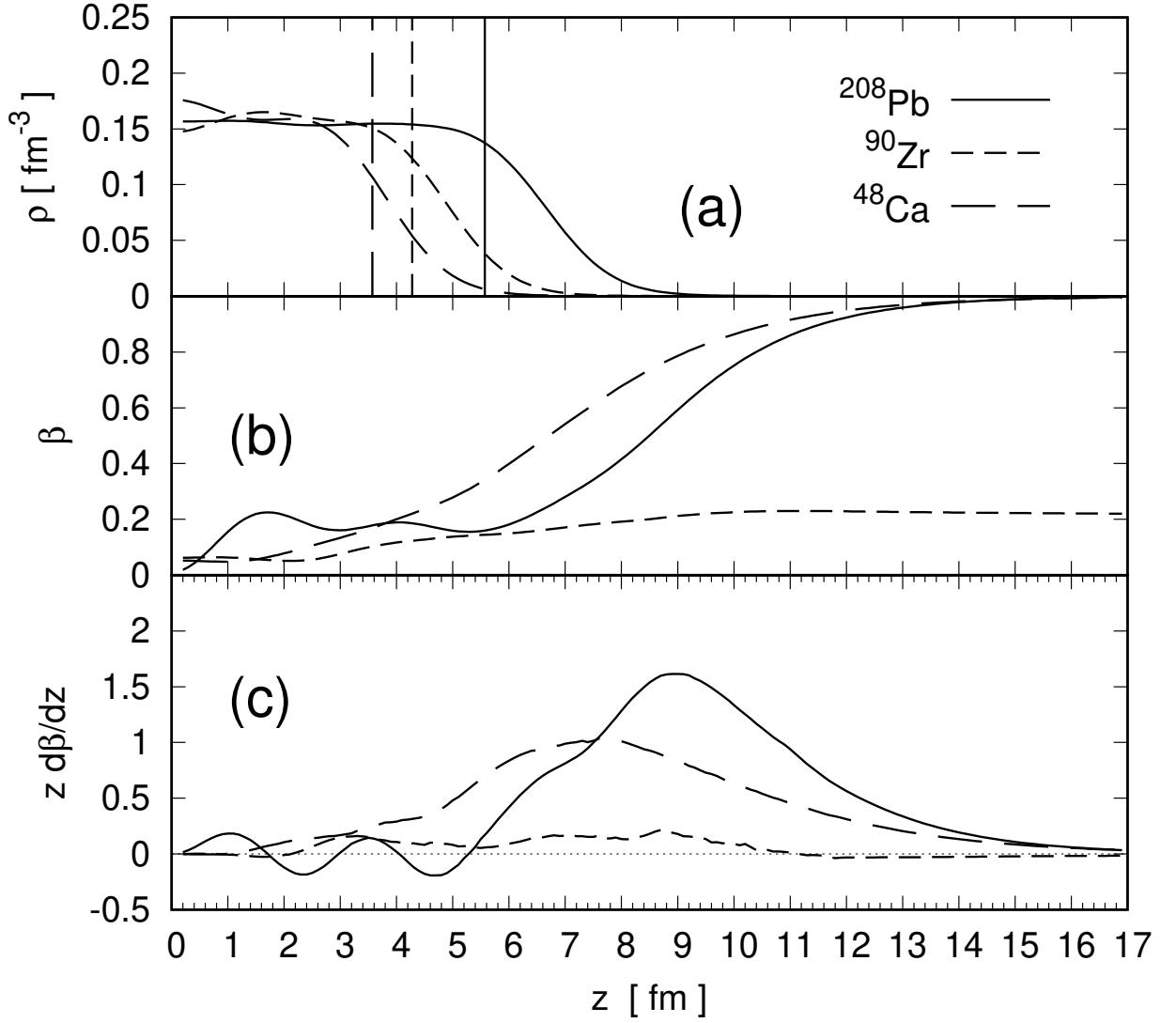


FIG. 1. Isoscalar density ρ , isospin asymmetry β and dimensionless gradient $z(\partial\beta/\partial z)$ as functions of the radial coordinate z for ^{208}Pb , ^{90}Zr , and ^{48}Ca . The vertical lines in panel (a) denote the rms radius for each nucleus.

with the summation over proton or neutron shells. For the nonlocal density matrix we adopt the following construction suited for closed-shell nuclei

$$\rho(\mathbf{r}', \mathbf{r}) = \sum_{nlj} (2l+1) R_{nlj}(r') R_{nlj}(r) P_l(\hat{\mathbf{r}}' \cdot \hat{\mathbf{r}}), \quad (19)$$

with P_l the Legendre polynomial of order l . For our purposes, it is convenient to represent the density matrix in momentum space. Therefore, we perform a double Fourier transform resulting in

$$\begin{aligned} \tilde{\rho}(\mathbf{p}', \mathbf{p}) &= \frac{1}{(2\pi)^3} \int d\mathbf{r} d\mathbf{r}' e^{i(\mathbf{r}' \cdot \mathbf{p}' - \mathbf{r} \cdot \mathbf{p})} \rho(\mathbf{r}', \mathbf{r}) \\ &= \sum_{nlj} (2j+1) \tilde{R}_{nlj}(p') \tilde{R}_{nlj}(p) P_l(\hat{\mathbf{p}}' \cdot \hat{\mathbf{p}}), \end{aligned} \quad (20)$$

where

$$\tilde{R}_{nlj}(p) = \sqrt{\frac{2}{\pi}} \int_0^\infty r^2 dr j_l(pr) R_{nlj}(r), \quad (21)$$

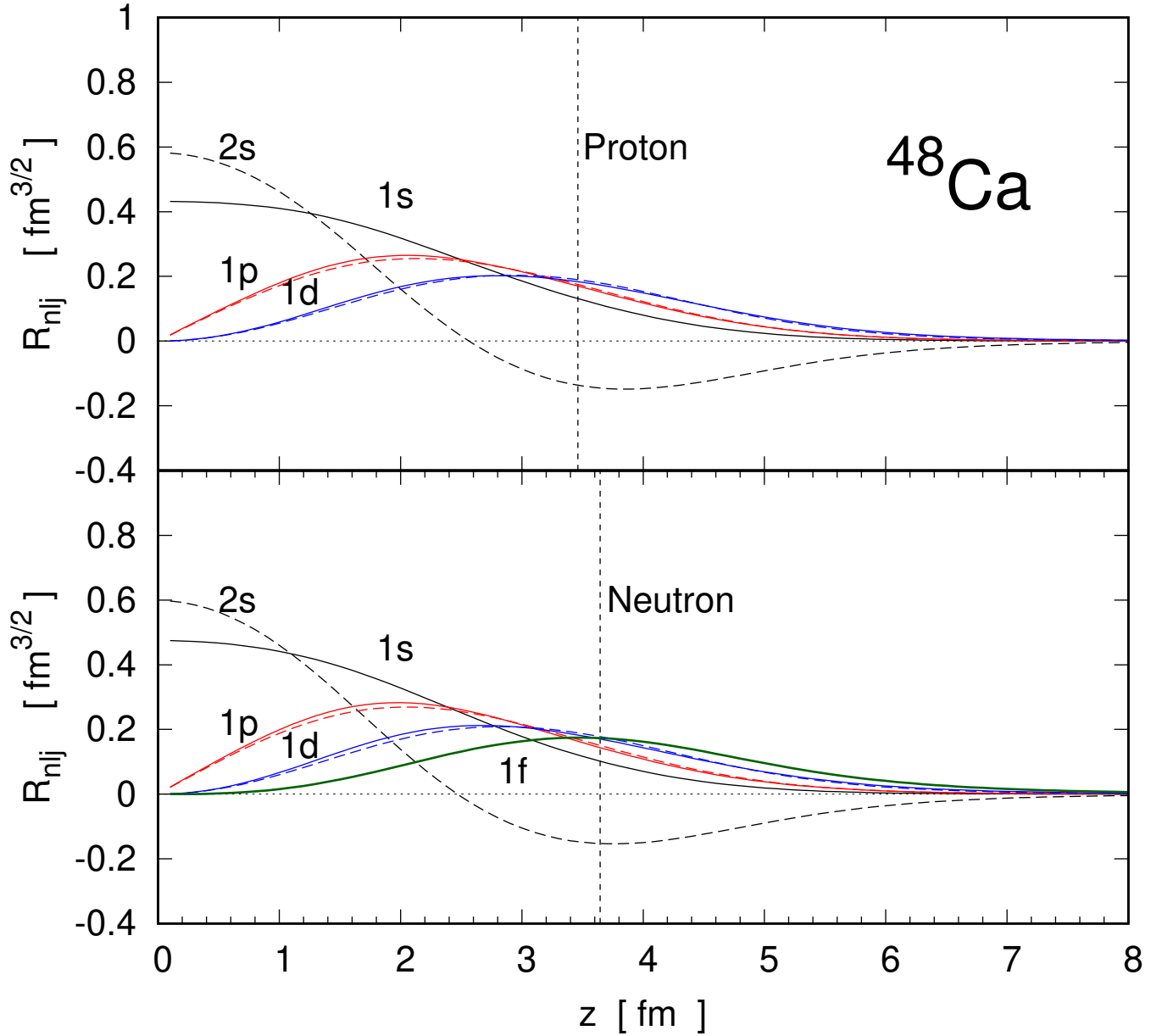


FIG. 2. Single-particle wavefunctions R_{nlj} for ^{48}Ca as functions of the radial coordinate z . Solid curves denote states with $j=|l-1/2|$, whereas dashed curves denote those with $j=l+1/2$.

with j_l the spherical Bessel function of the first kind, of order l . Let us now introduce $\mathbf{P} = \frac{1}{2}(\mathbf{p} + \mathbf{p}')$, and $\mathbf{Q} = \mathbf{p}' - \mathbf{p}$, so that $\mathbf{p}' = \mathbf{P} + \frac{1}{2}\mathbf{Q}$, and $\mathbf{p} = \mathbf{P} - \frac{1}{2}\mathbf{Q}$. Then

$$\tilde{\rho}(\mathbf{p}', \mathbf{p}) = \tilde{\rho}(\mathbf{P} + \frac{1}{2}\mathbf{Q}, \mathbf{P} - \frac{1}{2}\mathbf{Q}), \quad (22)$$

$$\equiv \tilde{\rho}(\mathbf{Q}; \mathbf{P}). \quad (23)$$

With this choice, the density matrix depends on the two vector momenta \mathbf{P} and \mathbf{Q} , where \mathbf{P} accounts for the commonly known Fermi motion, typically bound to about 1.5 fm^{-1} . If this momentum is summed over, we obtain the Fourier transform of the radial density $\rho(z)$, namely

$$\int \tilde{\rho}(\mathbf{Q}; \mathbf{P}) d\mathbf{P} = \tilde{\rho}(\mathbf{Q}), \quad (24)$$

which at $Q=0$ is normalized to the number of nucleons.

In this work, we find it useful to express the density matrix as a Legendre expansion in terms of $w = \hat{\mathbf{Q}} \cdot \hat{\mathbf{P}}$. Thus

$$\tilde{\rho}(\mathbf{Q}; \mathbf{P}) = \sum_n \tilde{\rho}_n(Q, P) P_n(w). \quad (25)$$

In practice,

$$\tilde{\rho}_n(Q, P) = \left(n + \frac{1}{2}\right) \int_{-1}^1 \tilde{\rho}(\mathbf{Q}; \mathbf{P}) dw, \quad (26)$$

with $w = \hat{\mathbf{Q}} \cdot \hat{\mathbf{P}}$, corresponding to the cosine of the angle between \mathbf{Q} and \mathbf{P} .

In Fig. 3 we present surface plots in the QP plane of the density matrix for ^{208}Pb . On the left-hand side (lhs) we plot the monopole term ($n = 0$). On the right-hand side (rhs) we show results for the density matrix in the Slater approximation [36] (see Appendix A). Red and green surfaces denote proton and neutron densities, respectively. We observe slight differences between the monopole (lhs) and Slater approximation (rhs) in their P dependence, with the Slater approximation featuring vanishing contributions above a given momentum P_{max} .

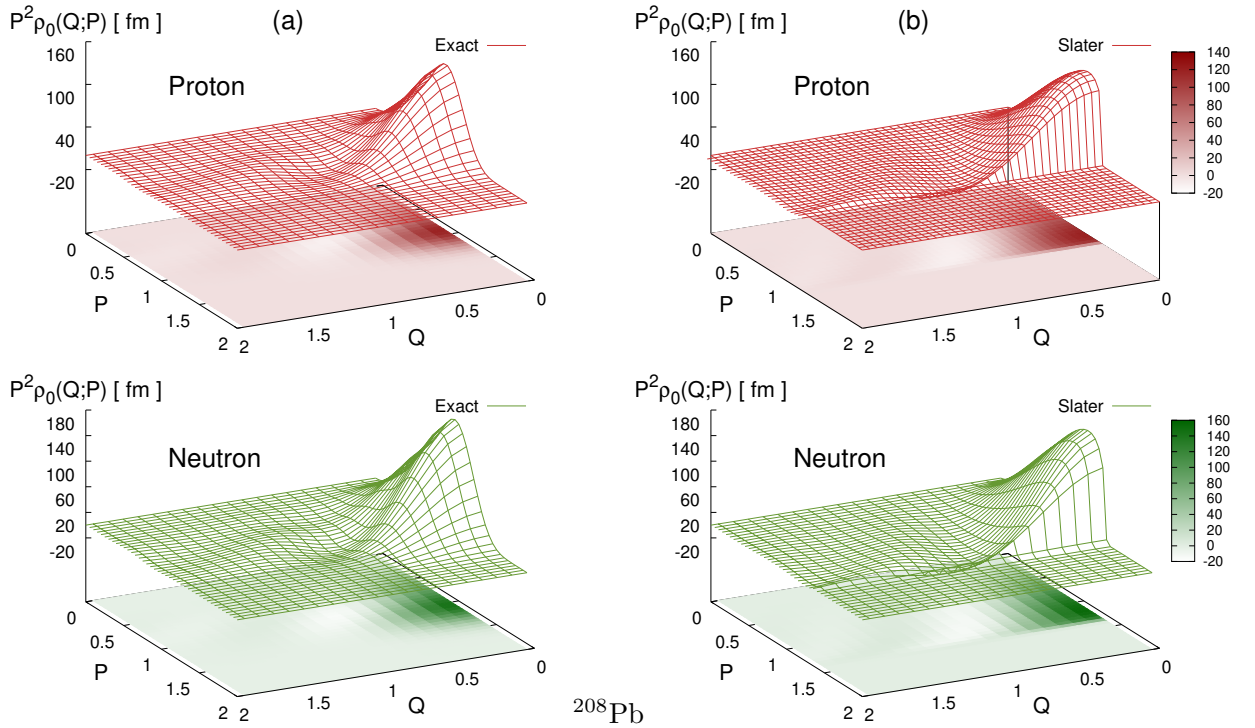


FIG. 3. Surface plots in the QP plane for proton and neutron densities in ^{208}Pb . Surfaces on the lhs correspond to the exact monopole density matrix, whereas on the rhs correspond to the Slater approximation.

B. In-medium g matrix

In order to represent the NN effective interaction at each radial coordinate z in the nucleus, we resort to the g matrix in the BHF approximation. This concept is an extension of the local density approximation proposed by Brieva and Rook [37]. In this work, we account for all non-localities of the interaction by retaining the intrinsic off-shell structure of the g matrix. Furthermore, at each coordinate z , we include the dependence of the g matrix on the local isoscalar density $\rho(z)$ and isospin asymmetry $\beta(z)$.

For infinite SNM or infinite PNM, the g matrix in the BHF approximation depends on the density ρ of the medium characterized by the Fermi momentum k_F and a starting energy ω . In this limit, when two-body correlations in the

ladder approximation are taken into account, the g matrix satisfies

$$\hat{g}(\omega) = \hat{v} + \hat{v} \frac{\hat{Q}}{\omega + i\eta - \hat{h}_1 - \hat{h}_2} \hat{g}(\omega), \quad (27)$$

with \hat{v} being the bare interaction between nucleons. Here \hat{h}_1 and \hat{h}_2 denote the s.p. energy of nucleons 1 and 2. The Pauli blocking operator \hat{Q} satisfies

$$\hat{Q}|\mathbf{p}\mathbf{k}\rangle = \Theta(p - k_F) \Theta(k - k_F) |\mathbf{p}\mathbf{k}\rangle. \quad (28)$$

Here $\Theta(x)$ represents the Heaviside step function. The solution to Eq. (28) enables the evaluation of the mass operator

$$M(\mathbf{k}; E) = \sum_{|\mathbf{p}| \leq k_F} \langle \frac{1}{2}(\mathbf{k} - \mathbf{p}) | g_{\mathbf{K}}(E + e_p) | \frac{1}{2}(\mathbf{k} - \mathbf{p}) \rangle_{\mathcal{A}}, \quad (29)$$

where \mathbf{K} is the total momentum of the interacting pair, $\mathbf{K} = \mathbf{k} + \mathbf{p}$, and

$$e_p = \frac{p^2}{2m} + U(p), \quad (30)$$

the s.p. energy defined in terms of an auxiliary field U . The nucleon mass m is taken as the average of proton and neutron masses. In the BHF approximation the s.p. potential is given by the real part of the on-shell mass operator, namely

$$U(k) = \Re M(k; e_k). \quad (31)$$

This imposes a self-consistency requirement, a condition which is achieved iteratively. In the continuous choice, this condition is imposed to all momenta k [38]. Further details on the way BHF solutions are obtained for this work can be found in Ref. [39].

In this study, we employ the AV18 NN potential [19] to represent the bare interaction. Solutions for the corresponding SNM and PNM have been reported in Refs. [39, 40]. In this case, the saturation point of SNM occurs at $k_F = 1.55 \text{ fm}^{-1}$. For these solutions, we obtain a slope parameter $L = 56.67 \text{ MeV}$, a value consistent with those reported by Danielewicz in Ref. [41]. The slope parameter is calculated from

$$L = 3\rho_0 \left. \frac{\partial S(\rho)}{\partial \rho} \right|_{\rho=\rho_0}. \quad (32)$$

with ρ_0 the saturation density. Here, $S(\rho)$ denotes the symmetry energy.

An appealing advantage of using the AV18 potential is that it describes NN observables up to energies of about 350 MeV. In Fig. 4 we plot the real (lhs) and imaginary part (rhs) of the on-shell mass operator based on AV18. We observe that the depth of the real part of the mass operator increases with the density. Additionally in both cases $U(k)$ crosses the axis around $k \approx 4 \text{ fm}^{-1}$. The imaginary part, on the other hand, vanishes for $k \leq k_F$, as expected. The thick solid curves correspond to s.p. solutions near the nuclear saturation density $\rho_0 = 0.16 \text{ fm}^{-3}$. We note that $U(k=0)$ for PNM is weaker by about 40% relative to SNM. These s.p. potentials are the ones used in Eq. (27) to obtain the off-shell elements $\langle \boldsymbol{\kappa}' | g(\omega; k_F) | \boldsymbol{\kappa} \rangle$ needed to evaluate $U(\mathbf{k}', \mathbf{k})$ in Eqs. (10a) and (10b).

C. Spin-isospin considerations

Here, we outline some general considerations made to incorporate the spin-isospin degrees of freedom in the NN effective interaction, which is generally denoted by t . In general terms, this operator can be expressed as

$$t = t_0 + t_\tau(\boldsymbol{\tau}_1 \cdot \boldsymbol{\tau}_2) + t_\sigma(\boldsymbol{\sigma}_1 \cdot \boldsymbol{\sigma}_2) + t_{\sigma\tau}(\boldsymbol{\sigma}_1 \cdot \boldsymbol{\sigma}_2)(\boldsymbol{\tau}_1 \cdot \boldsymbol{\tau}_2), \quad (33)$$

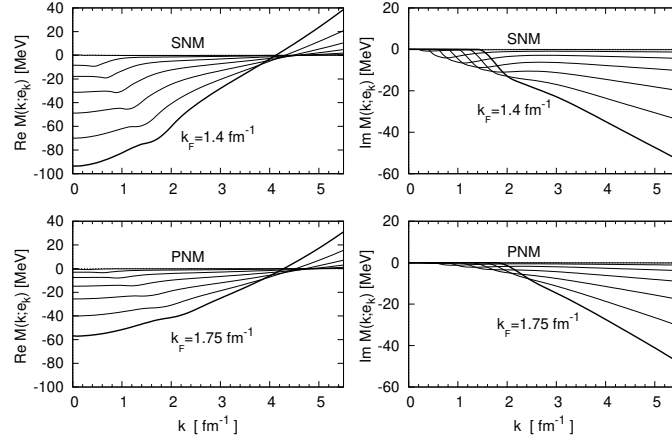


FIG. 4. On-shell mass operator $M(k; e_k)$ at different k_F as functions of k . Curves for SNM (upper frames) denote results with $0.4 \leq k_F \leq 1.4 \text{ fm}^{-1}$ in steps of 0.2 fm^{-1} , while those for PNM (lower frames) correspond to $0.5 \leq k_F \leq 1.75 \text{ fm}^{-1}$ in steps of 0.25 fm^{-1} .

where σ and τ denote Pauli matrices in spin and isospin spaces, with the subscripts 1, 2 referring to each nucleon. Here t_0 and t_τ denote the isoscalar and isovector components of the force. The total spin and isospin operators read

$$\mathbf{S} = \frac{1}{2}\sigma_1 + \frac{1}{2}\sigma_2, \quad (34a)$$

$$\mathbf{T} = \frac{1}{2}\tau_1 + \frac{1}{2}\tau_2, \quad (34b)$$

respectively. Thus, for the NN system the total spin S can be zero or one. The same for the isospin ($T = 0, 1$). In this basis each of the four components in Eq. (33) is given by

$$t_0 = \frac{1}{16}(T^{00} + 3T^{01} + 3T^{10} + 9T^{11}), \quad (35a)$$

$$t_\tau = \frac{1}{16}(-T^{00} + T^{01} - 3T^{10} + 3T^{11}), \quad (35b)$$

$$t_\sigma = \frac{1}{16}(-T^{00} - 3T^{01} + T^{10} + 3T^{11}), \quad (35c)$$

$$t_{\sigma\tau} = \frac{1}{16}(T^{00} - T^{01} - T^{10} + T^{11}), \quad (35d)$$

where we use the notation T^{ST} .

The terms involving the spin cancel out for nucleon scattering off closed-shell targets. For this reason, we pay attention to t_0 and t_τ . In the case of proton scattering, we need to couple it with the target protons or neutrons, which we denote by τ . If $\hat{\rho}_\tau$ denotes the density matrix of species τ , then the elements we need to incorporate in the construction of the optical potential are of the type $\langle p\tau | t | p\tau \rangle \hat{\rho}_\tau$. Then, the matrix elements of interest are of the type $\langle p\tau | t | p\tau \rangle$. Omitting the spin components of the force, we obtain the explicit expressions

$$\langle pp | t | pp \rangle = t_0 + t_\tau = \frac{1}{4}(T^{01} + 3T^{11}), \quad (36a)$$

$$\langle pn | t | pn \rangle = t_0 - t_\tau = \frac{1}{8}(T^{00} + T^{01} + 3T^{10} + 3T^{11}). \quad (36b)$$

We note that $\langle pp | t | pp \rangle = \langle nn | t | nn \rangle$, only contain isospin states $T = 1$, as it is shown in Eq. (36a).

In the calculation of proton-nucleus optical potentials we couple the projectile (proton) with target protons and target neutrons,

$$U_p = g_{pp} \otimes \rho_p + g_{pn} \otimes \rho_n. \quad (37)$$

Making explicit the β -dependence in the g matrix, as in Eq. (15), we get

$$U_p = (1 - \beta)g_{pp}^{(0)} \otimes \rho_p + \beta g_{pp}^{(1)} \otimes \rho_p + (1 - \beta)g_{pn}^{(0)} \otimes \rho_n + \beta g_{pn}^{(1)} \otimes \rho_n. \quad (38)$$

The corresponding gradient contribution becomes

$$\begin{aligned}
U_p^1 = & \left[(1 - \beta) \frac{\partial g_{pp}^{(0)}}{\partial z} - \frac{\partial \beta}{\partial z} g_{pp}^{(0)} \right] \otimes \rho_p + \\
& \left[(1 - \beta) \frac{\partial g_{pn}^{(0)}}{\partial z} - \frac{\partial \beta}{\partial z} g_{pn}^{(0)} \right] \otimes \rho_n + \\
& \left[\beta \frac{\partial g_{pp}^{(1)}}{\partial z} + \frac{\partial \beta}{\partial z} g_{pp}^{(1)} \right] \otimes \rho_p + \\
& \left[\beta \frac{\partial g_{pn}^{(1)}}{\partial z} + \frac{\partial \beta}{\partial z} g_{pn}^{(1)} \right] \otimes \rho_n .
\end{aligned} \tag{39}$$

In the case of neutron-nucleus optical potentials the coupling reads

$$U_n = g_{np} \otimes \rho_p + g_{nn} \otimes \rho_n, \tag{40}$$

with the resulting U_n^1 given analogous to that in Eq. (39).

IV. APPLICATIONS

In this section, we present and discuss the results for nucleon scattering from ^{208}Pb and ^{48}Ca at low and intermediate energies. First, we address the accuracy of the calculations in the context of the δg folding approach to subsequently assess the role of isospin asymmetry in the same context.

To calculate U_1 in Eq. (10b) one needs to evaluate the integral

$$z^3 \Omega(\mathbf{q}, \mathbf{P}; z) = \int d\mathbf{Q} \tilde{\rho}(\mathbf{Q}, \mathbf{P}) \frac{j_1(|\mathbf{Q} - \mathbf{q}|z)}{|\mathbf{Q} - \mathbf{q}|z}. \tag{41}$$

This is a delicate integral because it involves two functions that peak at different places. One at $Q = 0$, and the other at $\mathbf{q} = \mathbf{Q}$. In Appendix E we describe the method we developed to calculate this integral reliably. In our computational strategy, we make use of the multipole expansion of $\tilde{\rho}(\mathbf{Q}, \mathbf{P})$ of Eq. (26).

All NA potentials are calculated in momentum space. For this purpose, the infinite nuclear matter g matrices in the BHF approximation are calculated at twenty values of k_F uniformly distributed over 0 and 1.6 fm^{-1} for the SNM, and over 0 and 1.9 fm^{-1} for the PNM. See Refs. [39, 40] for further details. Additionally, shell-model s.p. wavefunctions for the targets are obtained from Ref. [35]. The resulting nonlocal NA potentials are then used to calculate their corresponding scattering observables for proton and neutron scattering, making use of the SWANLOP package [42, 43].

A. Folding in the Slater approximation: a test case

In the context of the δg folding, it is demonstrated in Refs. [14, 15] that if the density matrix is represented in the Slater approximation, the optical potential expressed by Eqs. (10a) and (10b) is reduced to the ABL folding of Eq. (11). This property becomes very useful for cross-checking the accuracy of the routines we have developed to incorporate the gradient term in U_1 .

As shown in Appendix D, for a given radial density $\rho(z)$ the density matrix in the Slater approximation becomes [44]

$$\tilde{\rho}_{\text{Slater}}(Q; P) = 4\pi \int_0^\infty z^2 dz j_0(Qz) \rho(z) n_z(P), \tag{42}$$

where

$$n_z(P) = \frac{1}{\frac{4}{3}\pi \hat{k}_z^3} \Theta(\hat{k}_z - P). \tag{43}$$

The local momentum \hat{k}_z is related to the proton or neutron local density $\rho(z)$ through

$$\rho(z) = \frac{\hat{k}_z^3}{3\pi^2}. \quad (44)$$

In this limit $U(\mathbf{k}', \mathbf{k})$ becomes the ABL folding, relying only on the radial density $\rho(z)$. We then replace the $\tilde{\rho}_{\text{Slater}}(Q; P)$ density matrix in the numerical calculation of U_1 . If the numerical implementation is consistent, the resulting potentials should match those from ABL.

In Fig. 5 we compare differential cross sections for optical potentials using the ABL folding (crosses) and the δg folding (solid curves) when the density matrix is represented in the Slater approximation. In this figure we consider ^{48}Ca and ^{208}Pb targets for proton at 40 and 200 MeV. We observe that the two results are identical to the eye.

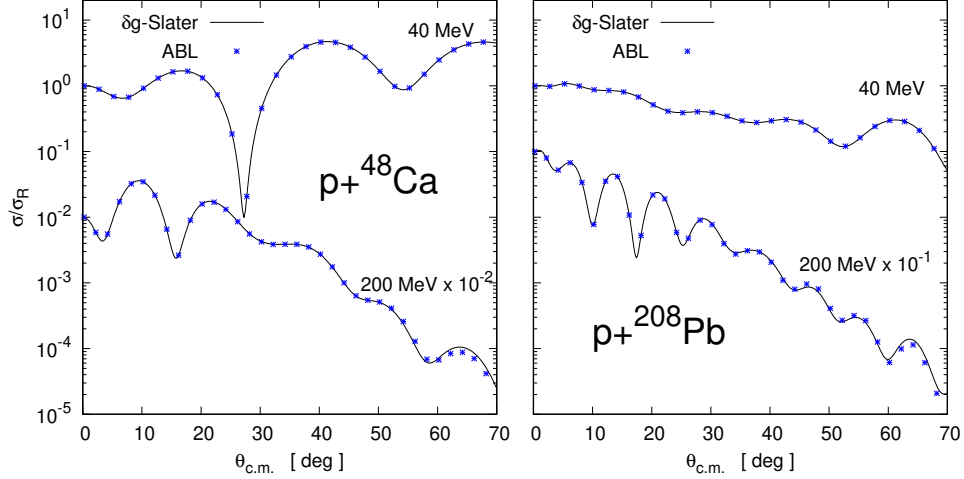


FIG. 5. Ratio-to-Rutherford differential cross section for proton elastic scattering from ^{48}Ca (lhs) and ^{208}Pb (rhs) at 40 MeV and 200 MeV, as functions of the c.m. scattering angle. Results at 200 MeV for ^{48}Ca and ^{208}Pb are multiplied by factors of 10^{-2} and 10^{-1} , respectively

In Table I we show the volume integral per nucleon (J/A) for $p+^{48}\text{Ca}$, and for $p+^{208}\text{Pb}$ scattering at 40 MeV. Here, we compare ABL and δg -folding results when the Slater approximation is used. We note that the differences between the ABL and the δg calculations are bound by 0.5% at the most, a reasonable discrepancy considering the many stages involved in the calculations.

TABLE I. Volume integral per nucleon for $p+^{48}\text{Ca}$, and $p+^{208}\text{Pb}$ scattering at 40 MeV.

	J/A [MeV fm ³]			
	^{48}Ca		^{208}Pb	
	Re	Im	Re	Im
ABL[$g^{(0)}$]	-704.5	-264.3	-701.4	-237.0
$\delta g[g^{(0)}]$	-707.2	-265.3	-702.5	-237.1
Difference	0.4%	0.4%	0.2%	0.1%
ABL[$g^{(0)}+g^{(1)}$]	-633.8	-220.9	-611.6	-188.2
$\delta g[g^{(0)}+g^{(1)}]$	-636.3	-220.7	-613.1	-187.4
Difference	0.4%	0.1%	0.2%	0.5%

B. δg folding with isospin-asymmetry

In this section, we focus on the role of the local isospin asymmetry $\beta(z)$ in nucleon elastic scattering considering two different approaches, with two variants each. The most complete approach is given by the δg folding, where the

nonlocal density matrix $\tilde{\rho}(\mathbf{Q}; \mathbf{P})$ is constructed explicitly from shell-model s.p. wavefunctions. The second approach is the ABL folding, an approximate scheme where the Slater approximation for the density matrix $\tilde{\rho}(\mathbf{Q}; \mathbf{P})$ is used. As a result, only radial densities $\rho_{p,n}(z)$ are needed. For each of these approaches, we consider β -dependent nuclear matter (denoted $g^{(0)} + g^{(1)}$) and SNM (denoted $g^{(0)}$).

In Fig. 6 we plot the measured and calculated differential cross section relative to Rutherford cross section σ/σ_R (a), analyzing power A_y (b) and spin rotation function Q (c) for proton scattering from ^{208}Pb at 40, 65 and 80 MeV beam energy. The data are from Refs. [45–50]. Black curves denote results based on δg -folding potentials whereas red curves represent those based on ABL approach. Additionally, solid curves denote calculations treating explicitly isospin asymmetry through $\beta(z)$, while dashed curves denote results using SNM for the g matrix.

To assess the role of isospin asymmetry at the level of the NN effective interaction, we pay attention to the low momentum results for the angular scattering observables, namely those with momentum transfer up to about 1.5 fm^{-1} . This criteria is motivated by the $t\rho$ structure of the optical potential, giving hints on the role of the two main inputs participating the construction of the potential: the target form factor and the effective interaction. Hence, if we assume better control on the effective interaction and the target densities at low q , then the low- q scattering observables would become more reliable. On the other end, the high-momentum behavior of the density $\tilde{\rho}(q)$ is more uncertain, therefore any disagreement between the model and the data can be attained to such uncertainties, in addition to higher order effects.

Results at 40 MeV in Fig. 6 exhibit clear differences between calculations including $g^{(1)}$ (solid curves) and excluding it (dashed curves) in the g matrix, feature observed at all angles. Additionally, the differences between δg - and ABL-folding approaches are relatively small. When comparing to the data we observe that the inclusion of $g^{(1)}$ favors an agreement with the data, feature more noticeable at momentum transfers $q \lesssim 1 \text{ fm}^{-1}$, for σ/σ_R and analyzing power A_y . At 65 MeV and 80 MeV we note the same tendency, although the role of $g^{(1)}$ becomes weaker as the energy increases.

Another feature also noted in Fig. 6 is the similarity between δg and ABL folding when the same considerations are applied to the g matrix. This indicates that the optical potential is not quite sensitive to the representation of the density matrix. This statement is valid as long as we use the same starting energy ω in the g matrix for each approach. As stated earlier, in this work we use as starting energy $\omega = E + \bar{e}$, with \bar{e} the nuclear-matter average s.p. energy at the local density $\rho(z)$. However, in a Hartree-Fock shell-model for the target each shell α has its corresponding s.p. energy ε_α . Hence, we should perform folding calculations for each shell in the nucleus, each one with its associated effective interaction at $\omega_\alpha = E + \varepsilon_\alpha$. Although this is an interesting issue to investigate, its implementation and study is computationally more demanding, beyond the scope of the present work.

In Fig. 7 we plot the measured [51, 52] and calculated ratio-to-Rutherford cross section σ/σ_R (a), analyzing power A_y (b) and spin rotation function Q (c) for proton elastic scattering from ^{48}Ca at 40 and 65 MeV beam energies. We follow the same convention for the curves as in Fig. 6. Here we also evidence better agreement between the data at 40 MeV and both folding approaches including $g^{(0)}$ and $g^{(1)}$, at momentum transfer $q \lesssim 1 \text{ fm}^{-1}$. In the case of 65 MeV, however, differences between the two approaches are less pronounced, implying weaker effects stemming from the isospin asymmetry at the level of the NN effective interaction.

We have also investigated $p + ^{90}\text{Zr}$ elastic scattering including and suppressing asymmetric nuclear matter contributions. In this case, the isospin asymmetry $\beta(z)$ for the target is rather small, as observed in Fig. 1. Note that in this case $\beta(z)$ is 0.2 at the most. Additionally, $\beta(z)$ is the smallest at the interior of the nucleus ($z < z_{rms}$), when compared with ^{208}Pb and ^{48}Ca . In Fig. 8 we show results for σ/σ_R , A_y and Q at beam energy of 40 MeV, an energy where we expect the effect of $g^{(1)}$ gets most pronounced. The curve textures follow the same convention as in Fig. 6. As observed, the differences between solid and dashed curves is quite moderate, with a slight shift of σ/σ_R to forward angles of the first diffractive minimum.

We have extended this study to higher energies. In Fig. 9 we plot the ratio-to-Rutherford differential cross section σ/σ_R (a), analyzing power A_y (b) and spin rotation Q (c), as functions of the scattering angle for proton elastic scattering from ^{208}Pb and ^{48}Ca . These results show that the inclusion of $g^{(1)}$ in the NN effective interaction results in marginal effects in the resulting scattering observables. This result is consistent with findings reported in Ref. [54] by Chinn *et al.*, where the Watson implementation of the multiple scattering expansion was contrasted with the KMT implementation, resulting in no visible differences at beam energies of 200 MeV and above.

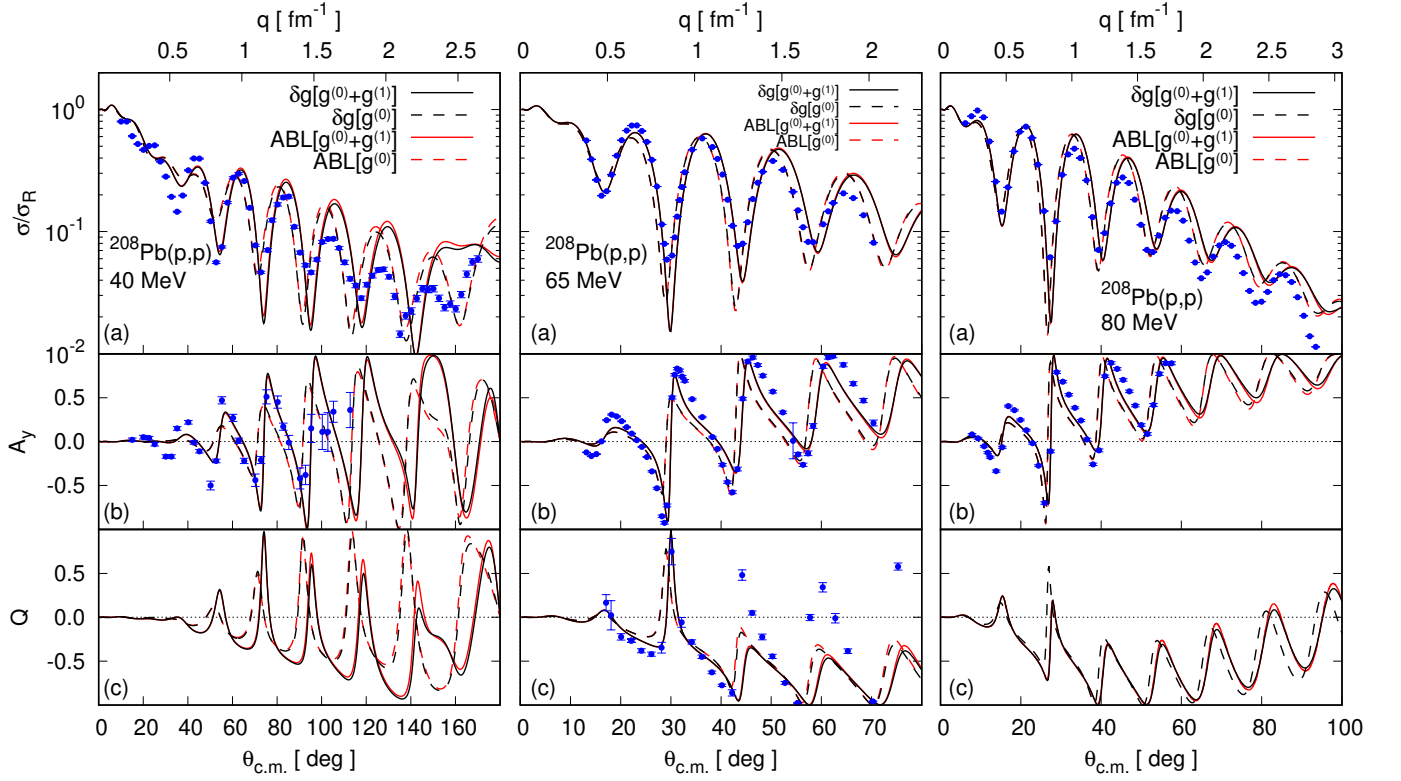


FIG. 6. Ratio-to-Rutherford differential cross section σ/σ_R (a), analyzing power A_y (b) and spin rotation function Q (c) for $p+^{208}\text{Pb}$ scattering at 40, 65, and 80 MeV, as a function of the c.m. scattering angle. The upper axis denotes momentum transfer q in units of fm^{-1} . The data are from Refs. [45–50]. Solid curves represent results from δg folding including both $g^{(0)}+g^{(1)}$. Dashed curves represent results considering only $g^{(0)}$ (SNM).

We now investigate the role of $g^{(1)}$ in the case of neutron scattering. In Figs. 10, 11, and 12 we show differential cross sections as functions of the scattering angle for $n+^{208}\text{Pb}$ elastic scattering at 40, 65 and 96 MeV, respectively. We follow the same convention for black and red curves as in Fig. 6. As in the cases of proton scattering, we observe small differences between δg and ABL folding approaches. Additionally, we also note that scattering at 40 MeV is more sensitive to the inclusion of the isovector part of the g matrix, feature which almost disappears at 96 MeV. The agreement with the data, however, is quite modest. At 40 MeV the calculated $d\sigma/d\Omega$ is much more diffractive than the data, at 65 MeV the calculated $d\sigma/d\Omega$ underestimates the data, whereas at 96 MeV the calculated $d\sigma/d\Omega$ appears more diffractive than the data. Whether these shortcomings have a common ground is an issue which remains to be investigated.

Total cross sections are among the properties of interest in NA scattering. In Table II we show the calculated elastic (σ_e), reaction (σ_R) and total (σ_T) cross section for neutron elastic scattering from ^{48}Ca and ^{208}Pb at 40 MeV. Here, we include all four approaches discussed in the preceding discussion. We observe that the overall discrepancy among all the calculated cross section is within 2 – 3%. In light of these results, we can state that ABL folding with SNM is a reasonable approach for calculating total cross sections, at least at energies at and above 40 MeV. The experimental value for the total cross section of $n+^{208}\text{Pb}$ at 40 MeV is 4.38 b [60]. The inclusion of $g^{(1)}$ in both approaches gets us closer to this value.

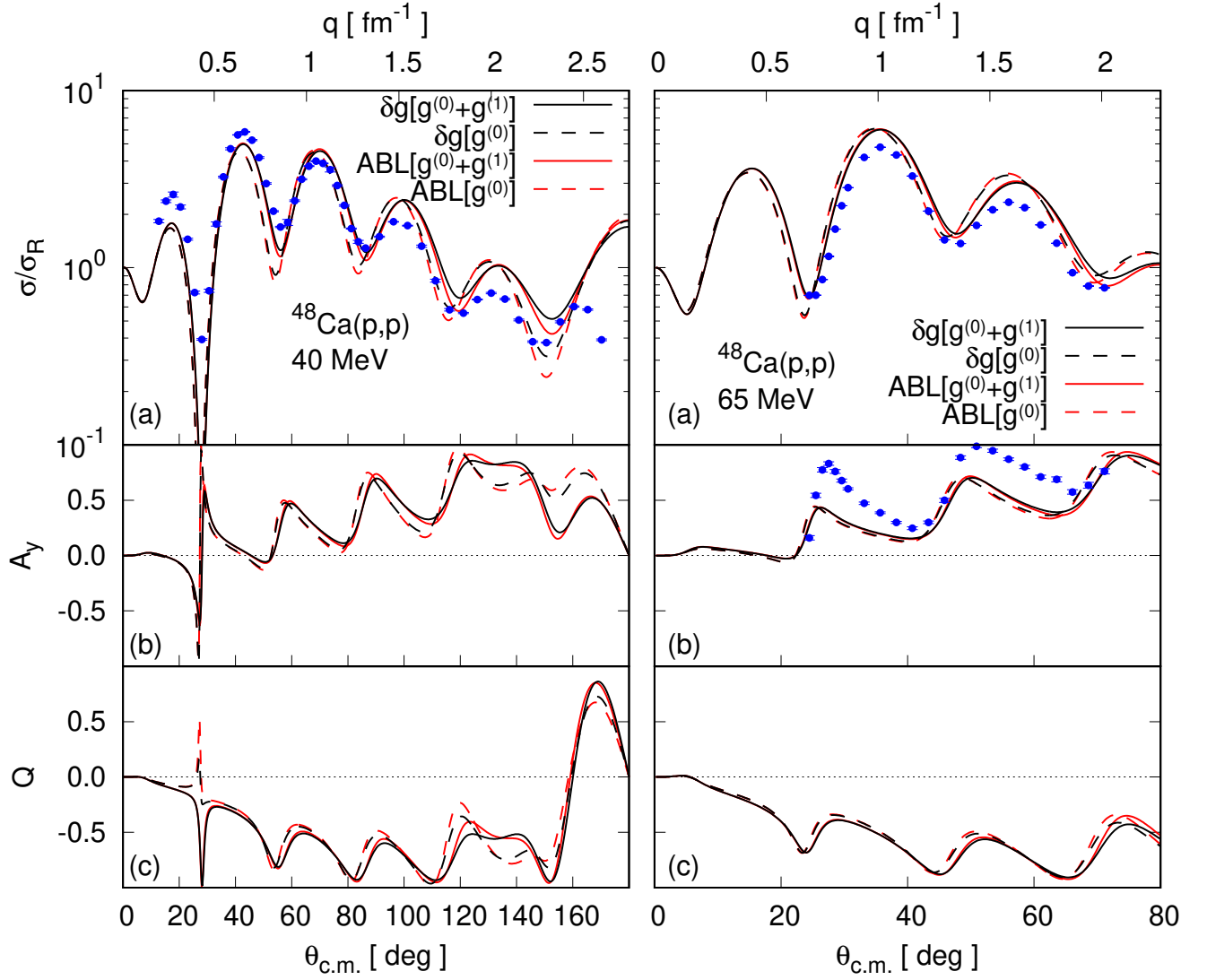


FIG. 7. Ratio-to-Rutherford cross section σ/σ_R (a), analyzing power A_y (b) and spin rotation function Q (c) for $p+^{48}\text{Ca}$ elastic scattering at 40 and 65 MeV. The data are from Refs. [51, 52]. Curve textures follow the same convention as in Fig. 6.

TABLE II. Calculated elastic, reaction and total cross section for $n+^{48}\text{Ca}$ and $n+^{208}\text{Pb}$ scattering at 40 MeV.

$n+^{48}\text{Ca}$	ABL		δg	
	$g^{(0)}$	$g^{(0)} + g^{(1)}$	$g^{(0)}$	$g^{(0)} + g^{(1)}$
σ_T [b]	2.19	2.17	2.17	2.15
σ_e [b]	1.13	1.17	1.12	1.16
σ_R [b]	1.06	1.00	1.05	0.994
$n+^{208}\text{Pb}$				
σ_T [b]	4.99	4.84	4.96	4.82
σ_e [b]	2.39	2.33	2.37	2.32
σ_R [b]	2.60	2.51	2.59	2.50

V. SUMMARY AND CONCLUSIONS

We have investigated the role of isospin asymmetry in the NN effective interaction in the context of NA elastic scattering. To this purpose we assume that the *in-medium* $g[\rho, \beta]$ matrix is an admixture of isospin-symmetric nuclear matter and pure neutron matter solutions of BHF equations, with a linear dependence on the asymmetry parameter

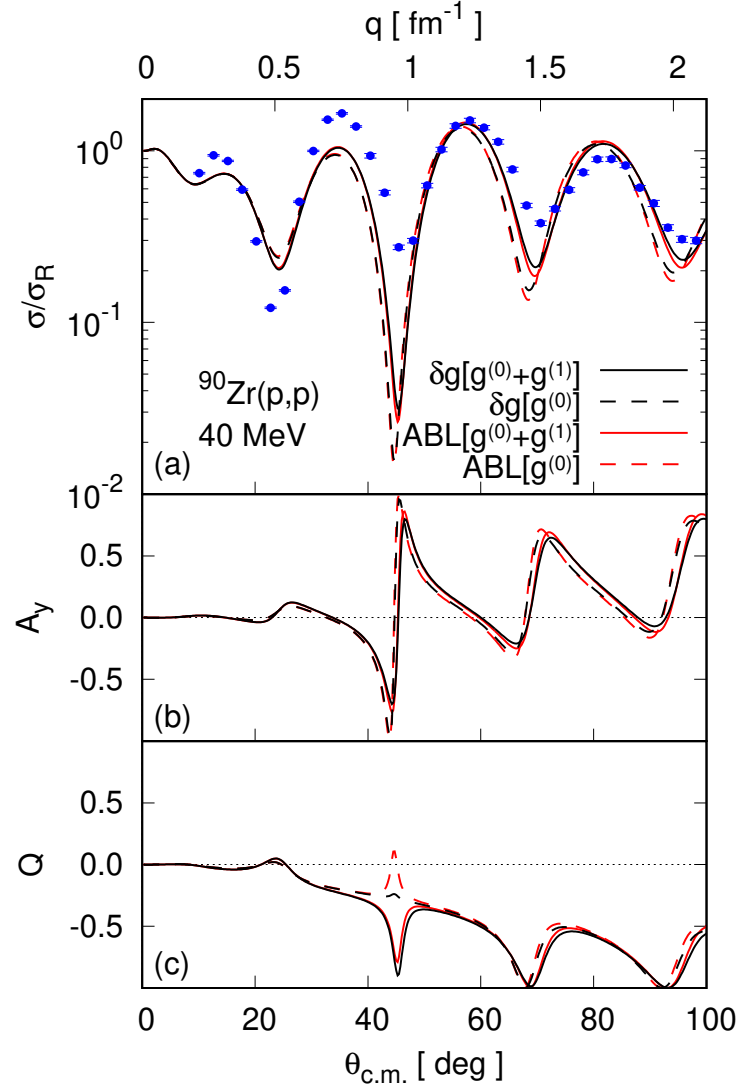


FIG. 8. Ratio-to-Rutherford cross section σ/σ_R (a), analyzing power A_y (b) and spin rotation function Q (c) for $p+^{90}\text{Zr}$ elastic scattering at 40 MeV. The data are from Refs. [53]. Curve textures follow the same convention as in Fig. 6.

β . This construction is supported by studies on asymmetric nuclear matter reported by Bombaci *et al.* [16]. We base this study on the Argonne v_{18} bare potential due to its ability to describe NN scattering up to 350 MeV. The isospin-asymmetric g matrices are then used for the construction of optical model potentials for elastic nucleon scattering off closed-shell nuclei. For this purpose, we make use of the δg folding approach introduced in Ref. [14], suited for an explicit treatment of the nonlocal density matrix. In this work, we make use of shell-model s.p. wavefunctions in a Hartree-Fock description of the ground state of nuclei. The folding approach we pursue provides us with a well-defined prescription to track the local isospin asymmetry throughout the target utilizing the *in-medium* $g[\rho, \beta]$ matrix. The calculated optical potentials are nonlocal, as all intrinsic nonlocalities in the g matrix are retained. Elastic scattering observables are obtained by employing the SWANLOP package [43], suited for nonlocal potentials in momentum space, including the Coulomb interaction.

We have found that the inclusion of isospin asymmetry in the g matrix, characterized through the local isospin asymmetry $\beta(z)$ and the inclusion of its isovector part, yields a reasonable description of differential cross sections at nucleon beam energies between 40 and 100 MeV. We also find that the use of the fully nonlocal density matrix, within the δg folding approach, yields similar results to those obtained within the ABL approach. This finding is useful in the sense that the calculation of optical potentials in the ABL approach is computationally less intensive than the δg folding approach. Thus, the ABL folding model constitute a safe starting approach to investigate NA collisions.

For proton scattering at energies of 65 MeV and below, the inclusion of $g^{(1)}$ yields better agreement with the scattering data at momentum transfers up to $\sim 1 \text{ fm}^{-1}$, relative to approaches based on SNM g matrices. The

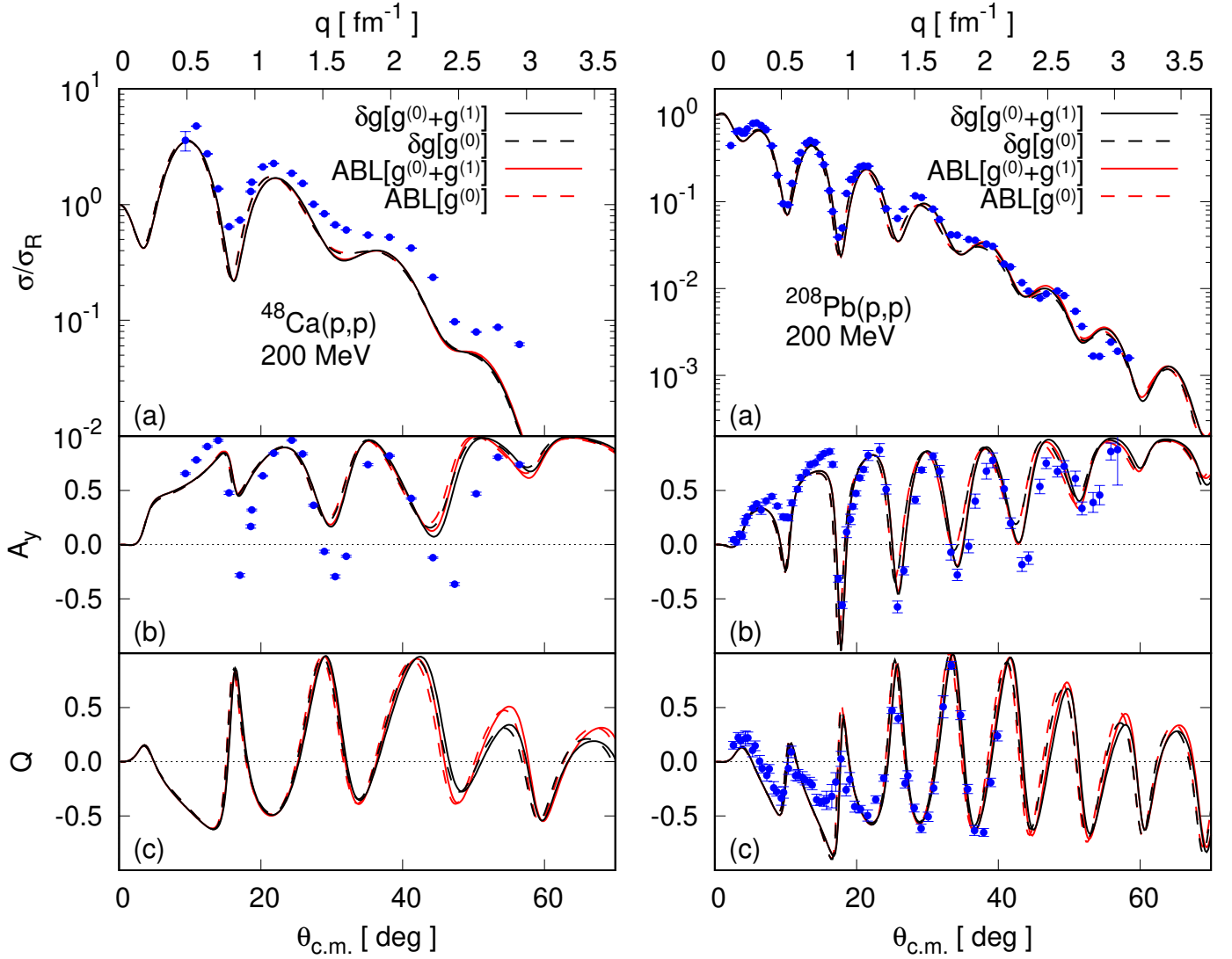


FIG. 9. Ratio-to-Rutherford differential cross section for $p+^{208}\text{Pb}$ and $p+^{48}\text{Ca}$ scattering at 200 MeV beam energy, as a function of the c.m. scattering angle. The data are from Refs. [55, 56].

physical implication of this result is that the isospin-asymmetry in the NN effective interaction is not negligible for a complete description of NA scattering at these energies. As the energy increases, the role of $g^{(1)}$ becomes weaker.

We conclude that the treatment of the local isospin asymmetry in the nucleus and associated site-dependent $g[\rho, \beta]$ matrix play an important role in the physics of collision processes involving isospin asymmetric targets. To assess the limits of these findings, it would be interesting to consider alternative bare NN interactions such as chiral potentials, and other solutions in the representation of the target ground state, in addition to open-shell nuclei as targets. An additional issue of interest is to investigate how the nonlocality of the optical potential gets expressed in its isovector component. In Ref. [61], the authors introduce the so-called $J\nu H$ universal factorization of the optical potential. The question would then be to characterize the nonlocality of the isovector term. These issues constitute natural extensions of this work.

ACKNOWLEDGMENTS

We are grateful to Prof. Ch. Elster for her valuable help in the preparation of this manuscript. The authors thank the referee for her/his thorough revision of the manuscript as well as asserted remarks and observations. H.F.A. acknowledges partial support provided by the supercomputing infrastructure of the NLHPC (ECM-02): Powered@NLHPC. He also thanks the hospitality of colleagues of CEA-DAM at Bruyères-le-Châtel, France, where part

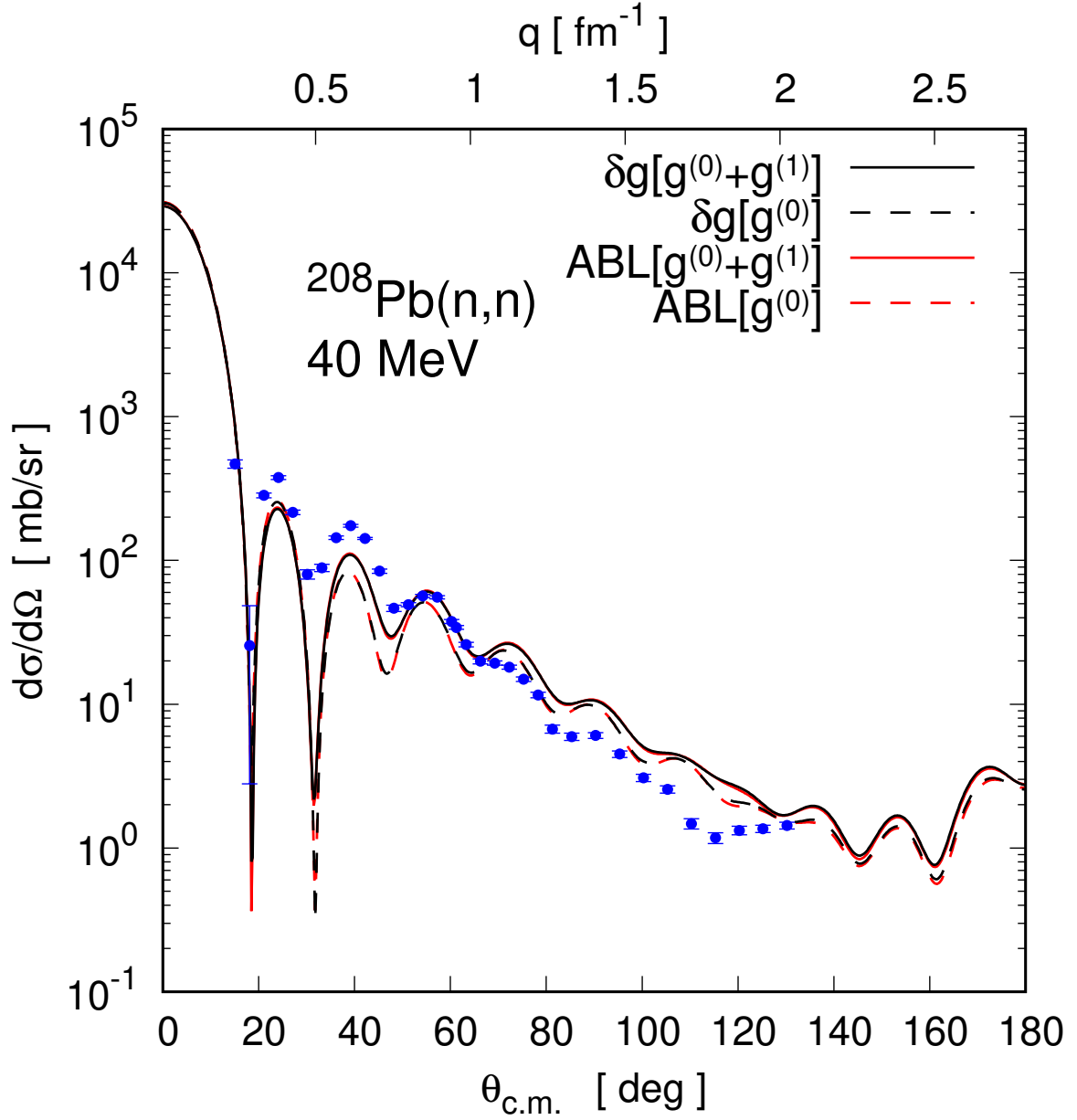


FIG. 10. Differential cross section for $n+^{208}\text{Pb}$ scattering at 40 MeV beam energy as a function of the c.m. scattering angle. The data are from Ref. [57].

of this work was done.

Appendix A: Slater approximation

The density matrix in a momentum representation $\tilde{\rho}(\mathbf{p}', \mathbf{p})$ can be related to its coordinate representation $\rho(\mathbf{r}', \mathbf{r})$ by a Fourier transform. In terms of the momentum variables defined by Eqs. (6) it can be shown that $\tilde{\rho}$ can be expressed as

$$\tilde{\rho}(\mathbf{P} + \frac{1}{2}\mathbf{Q}, \mathbf{P} - \frac{1}{2}\mathbf{Q}) = \frac{1}{(2\pi)^3} \int d\mathbf{z} d\mathbf{s} e^{i\mathbf{z}\cdot\mathbf{Q}} e^{i\mathbf{s}\cdot\mathbf{P}} \times \rho(\mathbf{z} + \frac{1}{2}\mathbf{s}, \mathbf{z} - \frac{1}{2}\mathbf{s}). \quad (\text{A1})$$

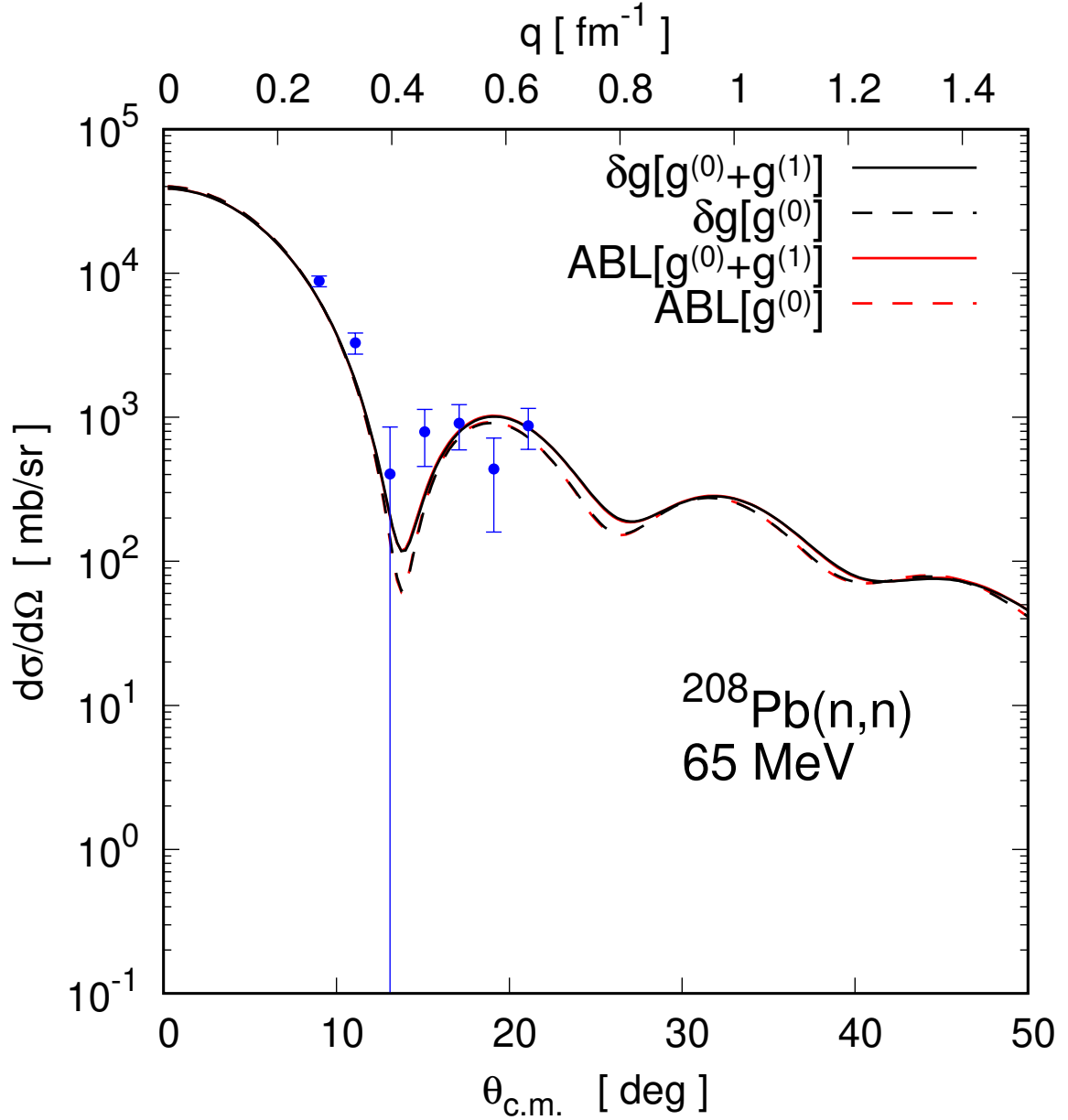


FIG. 11. Differential cross section for $n+^{208}\text{Pb}$ scattering at 65 MeV as a function of the c.m. scattering angle. The data are from Ref. [58].

In this expression \mathbf{z} refers to the mean struck-nucleon coordinate $(\mathbf{r} + \mathbf{r}')/2$, quantity denoted as \mathbf{R} in Ref. [36]. Additionally, \mathbf{s} represents the difference between \mathbf{r}' and \mathbf{r} .

Campi and Bouyssy [44] have shown that to a very good approximation, the density matrix in coordinate space for protons or neutrons can be cast in the Slater approximation as

$$\rho(\mathbf{z} + \frac{1}{2}\mathbf{s}, \mathbf{z} - \frac{1}{2}\mathbf{s}) \approx \rho(\mathbf{z}) F(\mathbf{z}; \mathbf{s}). \quad (\text{A2})$$

In this approximation, $\rho(\mathbf{z})$ represents the point density given by the diagonal terms of the coordinate-space density matrix, with $F(\mathbf{z}; \mathbf{s})$ being a measure of the non-locality of the density matrix. To ensure that the matter form factor is correctly reproduced, the condition $F(\mathbf{z}; 0) = 1$ must be satisfied. A feature implied by this approximation is the independence of the density matrix on the angle between \mathbf{z} and \mathbf{s} , resulting in an independence of $\tilde{\rho}$ on $\hat{\mathbf{Q}} \cdot \hat{\mathbf{q}}$ in Eq. (A1).

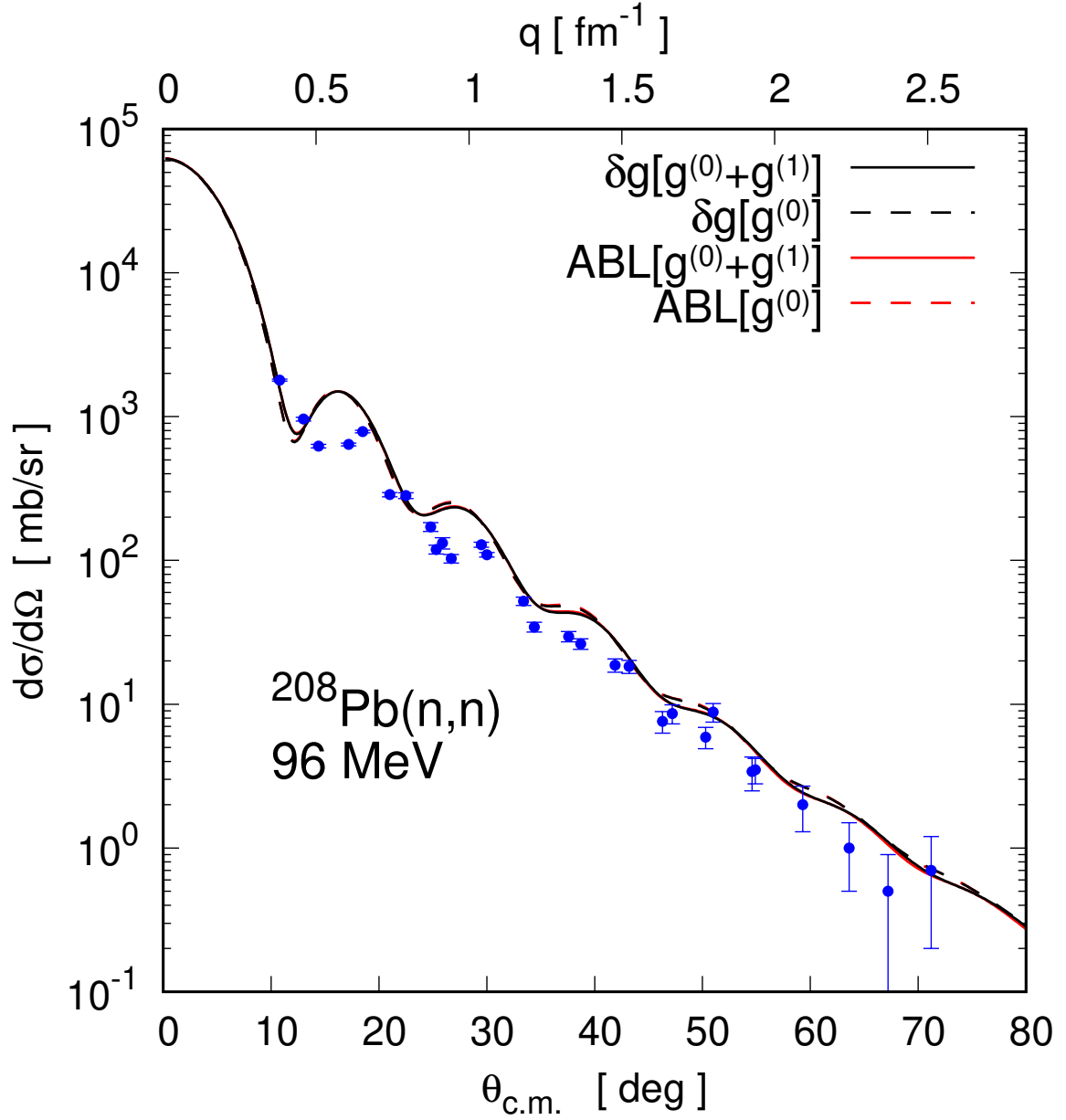


FIG. 12. Differential cross section for $n+^{208}\text{Pb}$ scattering at 96 MeV as a function of the c.m. scattering angle. The data are from Ref. [59].

Following Campi and Bouyssy, for $F(z; s)$ the structure suggested by nuclear matter, namely

$$F(z; s) = 3 \frac{j_1(\hat{k}(z) s)}{\hat{k}(z) s}, \quad (\text{A3})$$

is assumed, where j_1 is the spherical Bessel function of order 1. The choice for $\hat{k}(z)$ depends on the level of approximation required for the density matrix. The simplest choice corresponds to the Slater approximation

$$\hat{k}(z) \rightarrow \hat{k}_{\text{Slater}}(z) = [3\pi^2 \rho(z)]^{1/3}. \quad (\text{A4})$$

Thus, the momentum-space density matrix becomes

$$\tilde{\rho}(\mathbf{P} + \tfrac{1}{2}\mathbf{Q}, \mathbf{P} - \tfrac{1}{2}\mathbf{Q}) \approx \frac{1}{(2\pi)^3} \int dz e^{iz \cdot \mathbf{Q}} \rho(z) G(z; P), \quad (\text{A5})$$

where

$$G(z; P) = \int d\mathbf{s} e^{i\mathbf{s} \cdot \mathbf{P}} F(z; \mathbf{s}) . \quad (\text{A6})$$

Using Eq. (A4) for $\hat{k}(z)$ yields

$$G(z; P) = \frac{2}{\hat{\rho}(z)} \Theta[\hat{k}(z) - P] , \quad (\text{A7})$$

with $\hat{\rho}(z)$ given by

$$\hat{\rho}(z) = \frac{\hat{k}(z)^3}{3\pi^2} . \quad (\text{A8})$$

After substituting Eq. (A6) for $G(R; P)$ into Eq. (A1) we obtain $\tilde{\rho} \rightarrow \tilde{\rho}_{\text{Slater}}$, with $\tilde{\rho}_{\text{Slater}}$ expressed as

$$\tilde{\rho}_{\text{Slater}}(Q; P) = 4\pi \int_0^\infty z^2 dz j_0(Qz) \rho(z) n_z(P) , \quad (\text{A9})$$

where we have defined

$$n_z(P) = \frac{1}{\frac{4}{3}\pi \hat{k}_z^3} \Theta(\hat{k}_z - P) , \quad (\text{A10})$$

with $\hat{k}_z \equiv \hat{k}(z)$. Note that in this limit case the density matrix depends uniquely on the radial density $\rho(z)$.

Appendix B: Evaluation of $z^3 \Omega(\mathbf{q}, \mathbf{P}; z)$

In Eq. (41) we need to evaluate the three-dimensional integral

$$z^3 \Omega(\mathbf{q}, \mathbf{P}; z) = \int d\mathbf{Q} \tilde{\rho}(\mathbf{Q}; \mathbf{P}) \frac{j_1(|\mathbf{Q} - \mathbf{q}|z)}{|\mathbf{Q} - \mathbf{q}|z} , \quad (\text{B1})$$

where the density matrix $\tilde{\rho}(\mathbf{Q}; \mathbf{P})$ depends, in the general case, on the angle between $\hat{\mathbf{Q}}$ and $\hat{\mathbf{P}}$. We present here a method to evaluate it with accuracy. Let us express $\tilde{\rho}$ as a sum of multipoles of the form

$$\tilde{\rho}(\mathbf{Q}; \mathbf{P}) = \sum_n \tilde{\rho}_n(Q, P) P_n(w) , \quad (\text{B2})$$

with $P_n(w)$ being the Legendre polynomials and $w = \hat{\mathbf{Q}} \cdot \hat{\mathbf{P}}$. In addition, we recall the expression of the Fourier transform of a three-dimensional hard sphere, where

$$\int d\mathbf{x} \Theta(z - x) e^{i\mathbf{Q} \cdot \mathbf{x}} = 4\pi z^3 \frac{j_1(Qz)}{Qz} , \quad (\text{B3})$$

where Θ is the usual Heaviside step function. After replacing Eqs. (B2) for $\tilde{\rho}$ and Eq. (B3) for $j_1(t)/t$ into Eq. (B1) for $z^3 \Omega$ we obtain

$$z^3 \Omega(\mathbf{q}, \mathbf{P}; z) = \frac{1}{4\pi} \sum_n \int d\mathbf{Q} \int d\mathbf{x} \Theta(z - x) \times \\ e^{i(\mathbf{Q} - \mathbf{q}) \cdot \mathbf{x}} \tilde{\rho}_n(Q, P) P_n(\hat{\mathbf{Q}} \cdot \hat{\mathbf{P}}) . \quad (\text{B4})$$

Using spherical coordinates for \mathbf{x} , where $d\mathbf{x} = x^2 dx d\Omega_x$, the solid-angle integral in $d\Omega_x$ can be performed analytically. Indeed, after expanding in partial waves $e^{i\mathbf{Q} \cdot \mathbf{x}}$ and $e^{-i\mathbf{q} \cdot \mathbf{x}}$, the solid angle integration yields

$$\int d\Omega_x e^{i\mathbf{Q} \cdot \mathbf{x}} e^{-i\mathbf{q} \cdot \mathbf{x}} = 4\pi \sum_m (2m+1) j_m(Qx) j_m(qx) P_m(\hat{\mathbf{Q}} \cdot \hat{\mathbf{q}}) . \quad (\text{B5})$$

This is substituted in Eq. (B4), leading to

$$z^3 \Omega(\mathbf{q}, \mathbf{P}; z) = \sum_n \sum_m \int d\mathbf{Q} \int x^2 dx \Theta(z - x) \times \\ (2m + 1) j_m(Qx) j_m(qx) \times \\ \tilde{\rho}_n(Q, P) P_m(\hat{\mathbf{Q}} \cdot \hat{\mathbf{q}}) P_n(\hat{\mathbf{Q}} \cdot \hat{\mathbf{P}}) . \quad (\text{B6})$$

Considering the identity

$$\int d\hat{\mathbf{Q}} P_m(\hat{\mathbf{Q}} \cdot \hat{\mathbf{q}}) P_n(\hat{\mathbf{Q}} \cdot \hat{\mathbf{P}}) = \frac{4\pi}{2n + 1} P_n(\hat{\mathbf{q}} \cdot \hat{\mathbf{P}}) \delta_{nm} , \quad (\text{B7})$$

Eq. (B6) results in

$$z^3 \Omega(\mathbf{q}, \mathbf{P}; z) = 4\pi \sum_n \int Q^2 dQ \int x^2 dx \Theta(z - x) \times \\ j_n(Qx) j_n(qx) \times \tilde{\rho}_n(Q, P) P_n(\hat{\mathbf{q}} \cdot \hat{\mathbf{P}}) .$$

In this way, if we define the hybrid representation of the density matrix by

$$\bar{\rho}_n(x, P) = \int Q^2 dQ j_n(Qx) \tilde{\rho}_n(Q, P) , \quad (\text{B8})$$

and Eq. (B1) for $z^3 \Omega$ reduces to

$$z^3 \Omega(\mathbf{q}, \mathbf{P}; z) = 4\pi \sum_n \int_0^z x^2 dx j_n(qx) \bar{\rho}_n(x, P) P_n(\hat{\mathbf{q}} \cdot \hat{\mathbf{P}}) . \quad (\text{B9})$$

The advantage of this expression over that in Eq. (B1) is that it requires to perform only two well controllable integrals, avoiding the direct angular integration over the solid angle $d\Omega_Q$. This expression has been implemented in the computational codes to evaluate the gradient term of U_1 .

-
- [1] *MSU* (2021), url: <https://frib.msu.edu/>.
 - [2] *GSI* (2021), url: <https://www.gsi.de/en/researchaccelerators.htm>.
 - [3] *EURISOL* (2021), url: <http://www.eurisol.org/>.
 - [4] *ISOLDE* (2021), url: <http://isolde.web.cern.ch/>.
 - [5] *SPIRAL* (2021), url: <http://www.ganil-spiral2.eu/>.
 - [6] *RIKEN* (2021), url: https://www.nishina.riken.jp/index_e.html.
 - [7] J. Rotureau, P. Danielewicz, G. Hagen, F. M. Nunes, and T. Papenbrock, *Phys. Rev. C* **95**, 024315 (2017), arXiv:1611.04554 [nucl-th].
 - [8] A. Idini, C. Barbieri, and P. Navrátil, *Journal of Physics: Conference Series* **981**, 012005 (2018).
 - [9] M. Burrows, K. D. Launey, A. Mercenne, R. B. Baker, G. H. Sargsyan, T. Dytrych, and D. Langr, *Phys. Rev. C* **109**, 014616 (2024), arXiv:2307.00202 [nucl-th].
 - [10] M. Burrows, C. Elster, S. P. Weppner, K. D. Launey, P. Maris, A. Nogga, and G. Popa, *Phys. Rev. C* **99**, 044603 (2019).
 - [11] R. B. Baker, C. Elster, T. Dytrych, and K. D. Launey, *Phys. Rev. C* **110**, 034605 (2024), arXiv:2404.03106 [nucl-th].
 - [12] C. Hebborn, F. M. Nunes, G. Potel, W. H. Dickhoff, J. W. Holt, M. C. Atkinson, R. B. Baker, C. Barbieri, G. Blanchon, M. Burrows, R. Capote, P. Danielewicz, M. Dupuis, C. Elster, J. E. Escher, L. Hlophe, A. Idini, H. Jayatissa, B. P. Kay, K. Kravvaris, J. J. Manfredi, A. Mercenne, B. Morillon, G. Perdikakis, C. D. Pruitt, G. H. Sargsyan, I. J. Thompson, M. Vorabbi, and T. R. Whitehead, *Journal of Physics G: Nuclear and Particle Physics* **50**, 060501 (2023).
 - [13] W. Dickhoff and R. Charity, *Progress in Particle and Nuclear Physics* **105**, 252 (2019).
 - [14] H. F. Arellano and E. Bauge, *Phys. Rev. C* **76**, 014613 (2007).
 - [15] F. J. Aguayo and H. F. Arellano, *Phys. Rev. C* **78**, 014608 (2008).
 - [16] I. Bombaci and U. Lombardo, *Phys. Rev. C* **44**, 1892 (1991).
 - [17] Z. X. W. H. Q. Song and T. T. S. Kuo, *Phys. Rev. C* **46**, 1788 (1992).
 - [18] W. Zuo, I. Bombaci, and U. Lombardo, *Phys. Rev. C* **60**, 024605 (1999).
 - [19] R. B. Wiringa, V. G. J. Stoks, and R. Schiavilla, *Phys. Rev. C* **51**, 38 (1995).
 - [20] K. M. Watson, *Phys. Rev.* **89**, 575 (1953).

- [21] H. Feshbach, *Annals of Physics* **19**, 287 (1962).
- [22] A. Kerman, H. McManus, and R. Thaler, *Annals of Physics* **8**, 551 (1959).
- [23] A. L. Fetter and K. M. Watson, *Advances in Theoretical Physics*, edited by K. A. Brueckner (Academic Press, New York, 1965).
- [24] F. Villars, *Fundamentals in Nuclear Theory*, edited by A. de-Shalit and C. Villi ed. (IAEA, Vienna, 1967).
- [25] F. Brieva and J. Rook, *Nuclear Physics A* **291**, 317 (1977).
- [26] H. V. von Geramb, *The Interaction Between Medium Energy Nucleons in Nuclei* (American Institute of Physics, New York, 1983).
- [27] K. Amos, P. J. Dortmans, H. V. von Geramb, S. Karataglidis, and J. Raynal, *Advances in Nuclear Physics*, Advances in Nuclear Physics, Vol. 25 (Springer, New York, 2000).
- [28] H. F. Arellano, F. A. Brieva, and W. G. Love, *Phys. Rev. C* **52**, 301 (1995).
- [29] H. F. Arellano and E. Bauge, *Phys. Rev. C* **84**, 034606 (2011).
- [30] H. F. Arellano, F. A. Brieva, and W. G. Love, *Phys. Rev. Lett.* **63**, 605 (1989).
- [31] H. F. Arellano, F. A. Brieva, and W. G. Love, *Phys. Rev. C* **41**, 2188 (1990).
- [32] C. Elster, T. Cheon, E. F. Redish, and P. C. Tandy, *Phys. Rev. C* **41**, 814 (1990).
- [33] R. Crespo, R. C. Johnson, and J. A. Tostevin, *Phys. Rev. C* **41**, 2257 (1990).
- [34] M. Vorabbi, C. Barbieri, V. Somà, P. Finelli, and C. Giusti, *Phys. Rev. C* **109**, 034613 (2024).
- [35] J. W. Negele, *Phys. Rev. C* **1**, 1260 (1970).
- [36] H. F. Arellano, F. A. Brieva, and W. G. Love, *Phys. Rev. C* **42**, 652 (1990).
- [37] F. Brieva and J. Rook, *Nuclear Physics A* **291**, 299 (1977).
- [38] M. Baldo and A. Fiasconaro, *Phys. Lett. B* **491**, 240 (2000).
- [39] H. F. Arellano and J.-P. Delaroche, *Eur. Phys. Journal A* **51**, 7 (2015).
- [40] F. Isaule, H. F. Arellano, and A. Rios, *Phys. Rev. C* **94**, 034004 (2016).
- [41] P. Danielewicz and J. Lee, *Nuclear Physics A* **818**, 36 (2009).
- [42] H. F. Arellano and G. Blanchon, *Physics Letters B* **789**, 256 (2019).
- [43] H. F. Arellano and G. Blanchon, *Computer Physics Communications* **259**, 107543 (2021).
- [44] X. Campi and A. Bouyssy, *Physics Letters B* **73**, 263 (1978).
- [45] Blumberg, L. N. and Gross, E. E. and VAN DER Woude, A. and Zucker, A. and Bassel, R. H., *Physical Review* **147**, 812 (1966).
- [46] H. Sakaguchi, M. Nakamura, K. Hatanaka, T. Noro, F. Ohtani, H. Sakamoto, O. H., and S. Kobayashi, *Physics Letters, Section B* **99**, 92 (1981).
- [47] A. Nadasen, P. Schwandt, P. P. Singh, W. W. Jacobs, A. D. Bacher, P. T. Debevec, M. D. Kaitchuck, and J. T. Meek, *Physical Review, Part C, Nuclear Physics* **23**, 1023 (1981).
- [48] L. N. Blumberg, E. E. Gross, A. VAN DER Woude, A. Zucker, and R. H. Bassel, *Phys. Rev.* **147**, 812 (1966).
- [49] H. Sakaguchi, M. Nakamura, K. Hatanaka, T. Noro, F. Ohtani, H. Sakamoto, H. Ogawa, and S. Kobayashi, *Physics Letters B* **99**, 92 (1981).
- [50] P. Schwandt, H. O. Meyer, W. W. Jacobs, A. D. Bacher, S. E. Vigdor, M. D. Kaitchuck, and T. R. Donoghue, *Phys. Rev. C* **26**, 55 (1982).
- [51] R. H. McCamis, T. N. Nasr, J. Birchall, N. E. Davison, W. T. H. van Oers, P. J. T. Verheijen, R. F. Carlson, A. J. Cox, B. C. Clark, E. D. Cooper, S. Hama, and R. L. Mercer, *Physical Review, Part C, Nuclear Physics* **33**, 1624 (1986).
- [52] H. Sakaguchi, M. Nakamura, K. Hatanaka, A. Goto, T. Noro, F. Ohtani, H. Sakamoto, and S. Kobayashi, *Physics Letters, Section B* **89**, 40 (1979).
- [53] L. N. Blumberg, E. E. Gross, A. Van Der Woude, A. Zucker, and R. H. Bassel, *Physical Review* **147**, 812 (1966).
- [54] C. R. Chinn, Ch. Elster, and R. M. Thaler, *Phys. Rev. C* **47**, 2242 (1993).
- [55] A. E. Feldman, J. J. Kelly, B. S. Flanders, M. A. Khandaker, H. Seifert, P. Boberg, S. D. Hyman, P. H. Karen, B. E. Norum, P. Welch, Q. Chen, A. D. Bacher, G. P. A. Berg, E. J. Stephenson, S. Nanda, A. Saha, and A. Scott, *Physical Review, Part C, Nuclear Physics* **49**, 2068 (1994).
- [56] D. Hutcheon, W. Olsen, H. Sherif, R. Dymarz, J. Camerón, J. Johansson, P. Kitching, P. Liljestrånd, W. McDonald, C. Miller, G. Neilson, D. Sheppard, D. McDaniels, J. Tinsley, P. Schwandt, L. Swenson, and C. Stronach, *Nuclear Physics A* **483**, 429 (1988).
- [57] R. P. DeVito, D. T. Khoa, S. M. Austin, B. U. E. P., and B. M. Loc, *Physical Review, Part C, Nuclear Physics* **85**, 024619 (2012).
- [58] J. H. Osborne, F. P. Brady, J. L. Romero, J. L. Ullmann, D. S. Sorenson, A. Ling, N. S. P. King, R. C. Haight, J. Rapaport, R. W. Finlay, E. Bauge, J. P. Delaroche, and A. J. Koning, *Physical Review, Part C, Nuclear Physics* **70**, 054613 (2004).
- [59] A. Ohn, J. Klug, J. Blomgren, C. Gustavsson, P. Mermod, L. Nilsson, S. Pomp, M. Osterlund, U. Tippawan, A. Prokofiev, and G. Tutin (2007) p. 1023, conf.on Nucl.Data for Sci. and Technology, Nice 2007.
- [60] R. W. Finlay, W. P. Abfalterer, G. Fink, E. Montei, T. Adami, P. W. Lisowski, G. L. Morgan, and R. C. Haight, *Phys. Rev. C* **47**, 237 (1993).
- [61] H. F. Arellano and G. Blanchon, *Phys. Rev. C* **109**, 064609 (2024).